Quantitative criteria to design optimal permeable trailing edges for noise abatement

Journal of Sound and Vibration 485 (2020) 115596

Contents lists available at ScienceDirect

Journal of Sound and Vibration

journal homepage: www.elsevier.com/locate/jsv

Quantitative criteria to design optimal permeable trailing edges for noise abatement

Alejandro Rubio Carpio*, Francesco Avallone, Daniele Ragni, Mirjam Snellen, Sybrand van der Zwaag

Faculty of Aerospace, Delft University of Technology, Delft 2629HS, the Netherlands

ARTICLE INFO

Article history:
Received 9 December 2019
Revised 28 May 2020
Accepted 20 July 2020
Available online 21 July 2020

2019 MSC:
00-01
99-00

Keywords:
Trailing edge noise
Noise control
Porous materials

ABSTRACT

An experimental study on broadband noise scattered by permeable trailing edges with different pore arrangements is performed. A NACA 0018 airfoil with chord $c = 0.2$ m is investigated at chord-based Reynolds numbers ranging from 1.4×10^5 to 3.8×10^5 and angles of attack of 0.2 and 5.4 degrees. Noise emission from five 3D-printed perforated trailing-edge inserts, with channels normal to the chord, is measured with a microphone antenna. For comparison, inserts manufactured with metallic foams, with comparable flow permeability K but more tortuous pore paths, are also analysed. All the inserts have a permeable extension s equal to 20% of the chord ($s/c = 0.2$). It is shown that noise mitigation ΔL_p, computed as the difference between far-field noise scattering from solid and permeable edges, collapse when nondimensionalizing frequency as Strouhal number based on the chord. From the collapsed data, it is observed that the maximum noise attenuation reported for each insert $\Delta L_{p,\max}$ reaches an asymptotic value of 9.3 dB for increasing K. To parameterize such asymptotic behaviour, noise reduction levels are fitted to a newly proposed relation $\Delta L_{p,\max} = \gamma_1 \tanh(\gamma_2 K)$ (where γ_1 and γ_2 are fitting coefficients, that depend on the type of insert and angle of attack). Following this analysis, limit permeability values for perforated and metal foam inserts of $K = 3.5 \times 10^{-9}$ and 1×10^{-9} m^2 are found, respectively; above these thresholds, less than 1 dB additional noise mitigation is reported; below, a difference in $\Delta L_{p,\max}$ of up to 4 dB for a given K is measured depending on the pore organization. Consequently, the tortuosity of the permeable structure is identified as an additional parameter (to K) controlling noise attenuation. It is also observed that the acoustic performance of lower-permeability edges is less sensitive to changes in the angle of attack. Tests for permeable lengths equal to $s/c = 0.05$ and 0.1 are performed: the change of $\Delta L_{p,\max}$ with increasing s/c is also properly described with a hyperbolic tangent, evidencing equally good performance in noise reduction for all measured extents. Finally, for the most permeable insert with periodic pore arrangement, an extremely loud tonal noise caused by vortex shedding (+30 dB higher than broadband levels) from the blunt solid-permeable junction at $s/c = 0.8$ is reported. Since applying a longer permeable surface, or increasing the permeability at the trailing edge decreases the aerodynamic performance of the blade, a permeable trailing edge with $s/c = 0.05$, $K = 1 \times 10^{-9}$ m^2 and tortuosity of 1.15 is recommended to optimize broadband noise abatement and avoid shedding-related tones for the conditions explored in the current study.

* Corresponding author.
E-mail address: a.rubiocarpio@tudelft.nl (A. Rubio Carpio).

https://doi.org/10.1016/j.jsv.2020.115596

1. Introduction

Turbulent-boundary-layer trailing-edge noise is a significant contributor to noise generated by wind turbines [1], ventilation systems [2] or aircraft airframes [3]. This noise source is produced by turbulent eddies being diffracted at the aft edge of lifting devices [4]. The employment of permeable trailing edges can mitigate noise up to 25 dB [5] with respect to their equivalent solid configuration [6]. It is now well-established that permeable trailing edges mitigate the acoustic impedance jump at the edge, and promote noise scattering from different streamwise positions [7–9]. Such a process is controlled by the local permeability of the material [10], that determines the degree of flow communication between both sides of the airfoil (thus the magnitude of the acoustic impedance jump). Consequently, the employment of more permeable structures usually yields larger noise reduction [11].

Previous research on permeable trailing edges employed (open-cell) porous structures such as foams [12,13], sintered granulates [10], fiber felts [5] or metal meshes [14]. Materials with such a complex pore arrangement often entail additional fluid-dynamic and acoustic features. For instance, hydrodynamically rough surfaces produce high-frequency excess noise and increased turbulence levels close to the wall [15]; these effects might partially mask their acoustic benefits [9,11]. Further aspects, such as the change of properties when subject to conventional machining processes, or repeatability and inhomogeneity issues also discourage their use for research. Recently developed manufacturing techniques such as additive manufacturing (or 3D-printing) [16] allow constructing permeable trailing edges with channels that connect suction and pressure sides of the airfoil [17]. Consequently, edges with tailored permeability can be manufactured by varying hole size, shape or spatial density.

In the current manuscript, five different permeable trailing edges for a NACA 0018 are acoustically characterized at angles of attack α of 0.2 and 5.4 degrees and chord-based Reynolds numbers Re_c ranging between 1.8×10^5 and 4.5×10^5. These permeable edges, with straight channels normal to the chord, allow for flow communication between suction and pressure side along the last 20% of the airfoil. The five perforated inserts have the same hole diameter d_h but different permeability K, obtained by varying the spacing between holes l_h. Noise scattering of such perforated trailing edges, with a periodic channel arrangement, is compared to that of open-cell metal foam inserts, with different (random) micro-structure but similar macroscopic permeability. The comparison yields general criteria that might serve as guidelines for the design of future permeable trailing edges.

The current publication is organized as follows. The experimental set-up, the 3D-printed inserts and the acoustic phased array are described in Section 2. Then, far-field noise results are discussed in five subsections: firstly, scaling laws for noise mitigation with flow speed or material properties are presented in Section 3.1; the tortuosity of a permeable edge is proposed to further control and optimize noise abatement in Section 3.2; the scaling of far-field acoustic pressure with flow speed is reported in Section 3.3; a brief analysis on the effect of varying the chordwise permeable length on noise mitigation is presented in Section 3.4; finally, the origin of a tone measured for the most permeable perforated insert is addressed in Section 3.5. To conclude, in Section 4 a summary of the main findings is presented.

2. Experimental set-up

2.1. Wind tunnel and model

Experiments are carried out in the aeroacoustic vertical open-jet wind tunnel (A-Tunnel) at Delft University of Technology. The rectangular cross-section at the nozzle outlet is 0.4×0.7 m^2 (contraction ratio equal to 15:1). For the present investigation, experiments are performed at free-stream velocities of 12.5, 15, 20, 25, 30 and 34 m/s. Inflow conditions at the exit section are characterized by means of a Pitot tube and constant temperature anemometry (*Dantec Dynamics* P11 probe; *TSI IFA* 300 bridge). The streamwise velocity is uniform within 0.6% at the measured cross-section, and the turbulence intensity is below 0.06% for the range of free-stream velocities specified above.

A modular NACA 0018 airfoil with chord $c = 200$ mm and span $L = 400$ mm (Fig. 1(a–c)) is placed at the potential core of the jet with the leading edge 500 mm downstream the nozzle outlet. The model is installed between two wooden side plates (with height equal to 1.2 m) flush-mounted to the nozzle outlet (Fig. 1(d)). The high span-to-chord ratio $L/c = 2$ suggests that three-dimensional flow effects are negligible along the midspan line; this aspect is further confirmed by the good agreement between experimental boundary layer data obtained with the same set-up [9], XFOIL data [18] and high-fidelity simulations on a two-dimensional model [19].

The aluminium body of the airfoil is manufactured with numerical control machining (surface roughness: 0.05 mm). The last 20% of the airfoil can be replaced by permeable inserts made of different materials and permeability patterns. The inserts are simply attached to the airfoil by a dovetail construction, and their surface is flush to the solid airfoil surface. A piece of Scotch Crystal Tape (width: 19 mm; nominal thickness: 51 μm) is carefully applied at the junction between the

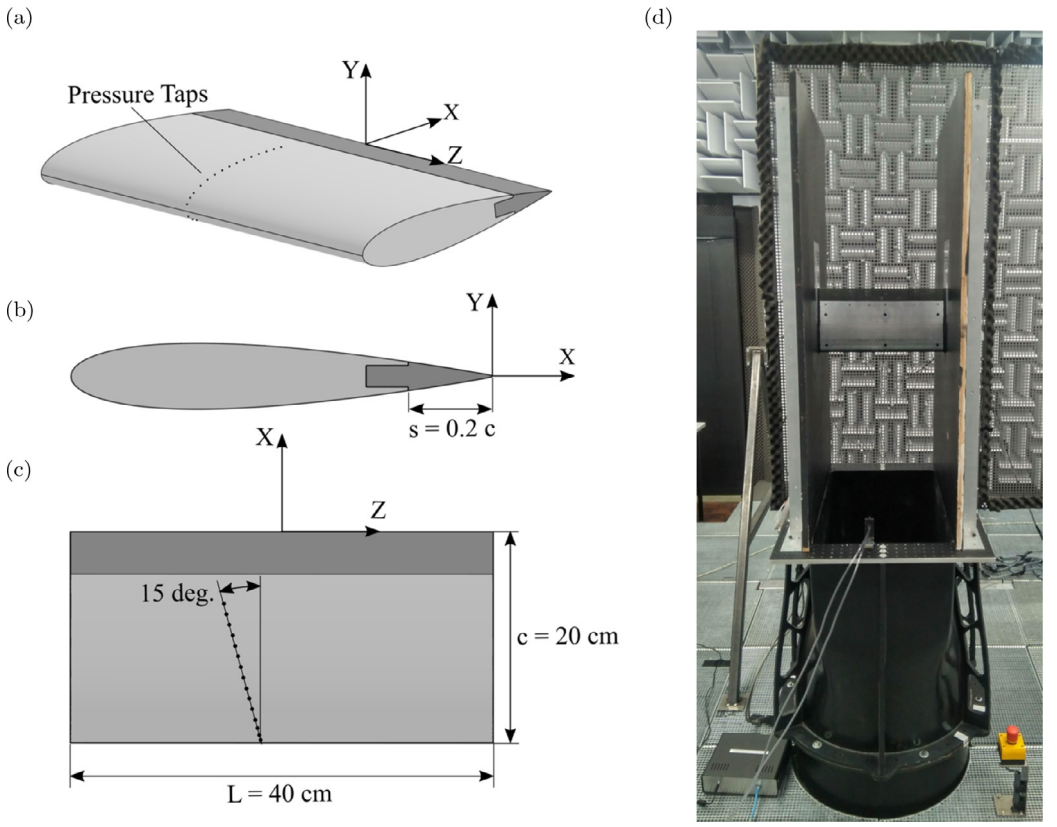

Fig. 1. Experimental set-up. The aluminium body of the airfoil is depicted in light grey. The exchangeable trailing-edge insert in dark grey. (a) 3-dimensional isometric view. (b) Side view. (c) Front view. (d) Picture of model and side plates assembled on the nozzle.

solid body of the airfoil and the permeable/solid trailing-edge inserts in such a way that the tape covers 1 mm of the insert in the streamwise direction. This procedure ensures a smooth transition between both pieces. The trailing-edge inserts have a thickness of 15.7 mm at the root and 0.3 mm at the tip.

Boundary-layer transition to turbulence is forced at 20% of the chord on both sides of the airfoil. The tripping device, with a chordwise extent of 10 mm, has 0.84 mm-height carborundum elements randomly distributed along the entire span. The turbulent state of the boundary layer is confirmed by scanning the airfoil surface with a *Brüel* & *Kjaer* (B&K) 4134 microphone connected to a B&K 2619 preamplifier.

The streamwise-vertical-spanwise $X - Y - Z$ coordinate system, employed in the remaining of the manuscript, is also depicted in Figs. 1(a–c). Its origin is located at the intersection between the midspan plane and the trailing edge, X and Z axes are respectively aligned with chord and trailing edge, and the Y axis points to the microphone antenna.

2.2. 3D-Printed trailing edges

Channelled trailing-edge inserts are manufactured with an *EnvisionTEC*'s Perfactory 4 Standard (resolution: 25 µm), a Digital Light Projector (DLP) printer. The inserts (surface roughness: 0.03 mm) are printed from root to tip using *EnvisionTEC*'s HTM 140 V2, a high-temperature photopolymer [20]. The total chordwise length of the inserts is 60 mm, of which only $s/c = 0.2 = 40$ mm are exposed to the flow (Fig. 1(b)). The maximum span of each insert is limited by the build envelope of the printer ($160 \times 100 \times 180$ mm^3) to 100 mm; hence, 4 inserts are assembled to build the entire trailing edge.

The inserts contain straight cylindrical channels normal to the chord connecting suction and pressure side. Holes are distributed according to a staggered square lattice, as shown in Fig. 2. In the present investigation, d_h is equal to 0.8 mm to ensure that the channels are open after the printing process and to avoid low-frequency acoustic tones [11]. The flow permeability K of the inserts is thus varied by changing the hole spacing l_h. Five different perforated inserts, with homogeneous hole spacing l_h of 1.5, 2, 2.5, 3 and 5 mm, are studied in the present manuscript. Hole spacings are chosen in order to obtain perforated edges with similar permeability to those manufactured with metallic foams (the permeability characterization is discussed more in detail later in Section 2.3). The smallest hole spacing ($l_h = 1.5$ mm) is determined by manufacturing constraints to guarantee 0.3 mm of solid material between orifices, which yields a satisfactory outcome of the 3D-printing process. Pictures of the inserts with $l_h = 1.5$ and 5 mm are shown in Fig. 3(a) and (b) respectively.

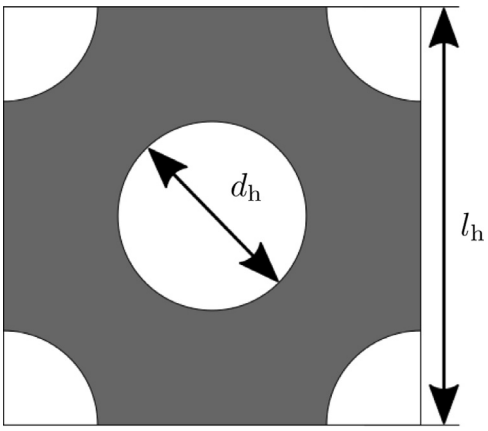

Fig. 2. Sketch of the hole pattern for perforated inserts.

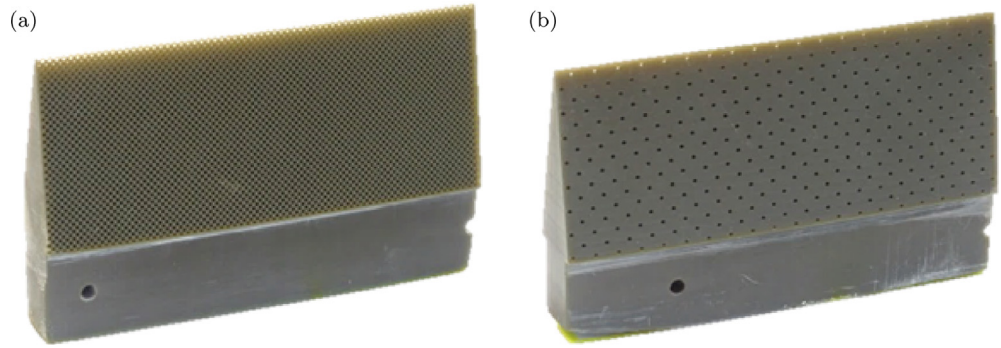

Fig. 3. Pictures of the 3D-printed trailing edges. Total chordwise length is 60 mm (of which exposed to the flow $s/c = 0.2 = 40$ mm). Total span is 100 mm. (a) $l_h = 1.5$ mm. (b) $l_h = 5$ mm. Note that a wavy edge results from the $l_h = 1.5$ mm hole distribution. A similar feature can be found in mock-ups with $l_h = 2$, 2.5 and 3 mm..

After the printing process it is observed that holes are not perfectly round due to limitations in the manufacturing technique [21]; specifically, the most downstreamwise end of each hole is flattened, producing D-shaped channels. Optical microscopy (Fig. 4) shows that these holes have a major diameter of approximately 800 µm and a shortened side with length of 700 µm. To account for this feature, an equivalent hole diameter of 754 µm, that yields a circle with area equal to the measured open area (of 447000 µm^2), is employed in Section 2.3.

2.3. Flow permeability and form coefficient

Flow permeability K and form coefficient C of trailing-edge inserts are determined by measuring the static pressure drop Δp across perforated samples with similar hole distributions. The pressure drop across a sample of permeable material is determined by the Hazen-Dupuit-Darcy equation [22]

$$\frac{\Delta p}{t} = \frac{\mu}{K} v + \rho C v^2 \tag{1}$$

where t is the thickness of the sample, ρ is the fluid density, μ is the dynamic viscosity and v is the Darcian velocity (defined as the ratio of volumetric flow rate to sample cross-section area). To characterize the two hydraulic properties (K and C) of each hole pattern, 4 cylindrical samples with thickness $t = 10$ mm, representative of the average trailing-edge insert thickness, are manufactured. These samples have hole patterns with $l_h = 1.5$ (Fig. 5(a)), 2.8, 4.5 and 6 mm ((Fig. 5(b))), and an outer diameter of 55 mm. To yield the same D-shaped hole feature, samples are printed as the trailing-edge inserts, i.e., the printing direction is perpendicular to the channels' axes. K and C are then computed by least-squares fitting of Eq. (1) to 20 pressure drop data, measured for Darcian velocities ranging between 0 and 1.1 m/s [23].

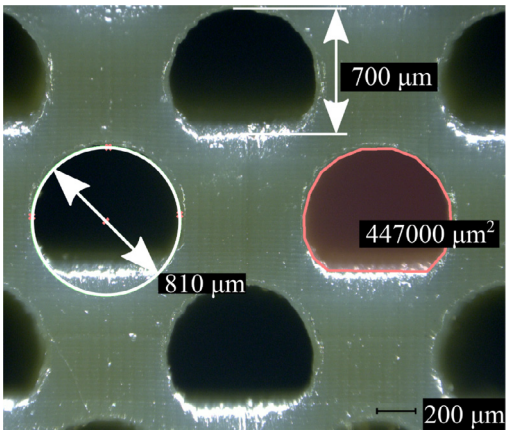

Fig. 4. Microscope picture of the perforated plate with $l_h = 1.5$ mm employed to characterize the hydraulic properties of the hole pattern. Hole open area is shadowed in red. Printing layers are distributed horizontally. Printing direction goes from top to bottom. For trailing-edge inserts air flows from top to bottom. Dimension: 1278 × 1114 px^2. Resolution: 2 µm/px. (For interpretation of the references to colour in this figure legend, the reader is referred to the web version of this article.)

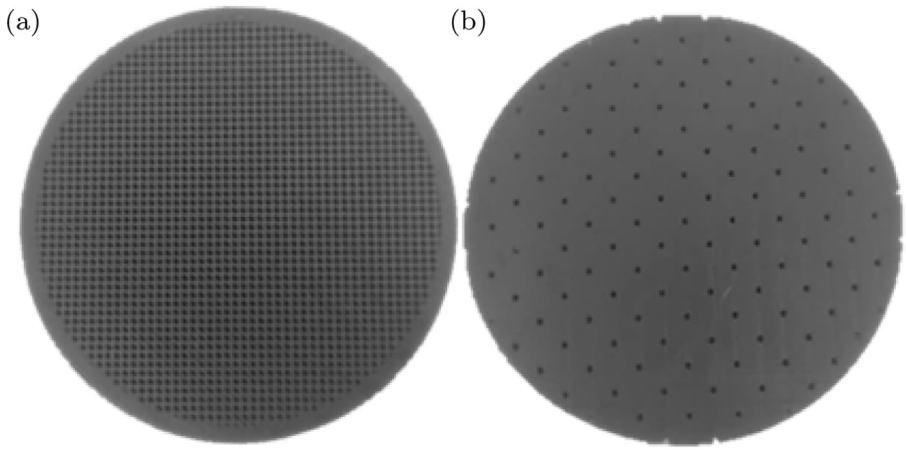

Fig. 5. Pictures of the 3D-printed cylindrical samples employed to characterize flow permeability and form coefficient of the different hole distributions. (a) $l_h = 1.5$ mm. (b) $l_h = 6$ mm.

Table 1
Fitting coefficients for Eq. (2)(a) and (b).

Study	β_1	β_2	β_3	R^2
Bae and Kim [24]	32	15	0.75	0.98
Present	40	15	0.73	0.95

Hydraulic properties for the hole distributions employed in the trailing edges are then estimated using Eq. (2)(a) and (b),

$$K = \frac{\sigma\, d_h^2\, t}{\beta_1 t + \beta_2 d_h} \tag{2a}$$

$$C = \beta_3 \frac{1-\sigma}{\sigma^2 t} \tag{2b}$$

where $\sigma = \pi d_h^2/(2l_h^2)$ is the porosity, defined as the ratio of fluid to solid volume. These empirical correlations are defined by Bae and Kim [24] for perforated plates with a similar hole arrangement and fully cylindrical holes. The original fit coefficients β_1, β_2 and β_3, as well as the ones retrieved with present data, are reported in Table 1. To validate the results, correlations based on measured data are compared to the ones presented by Bae and Kim [24] in Fig. 6(a) and (b). For completeness, K and C values computed from Eq. (1) (referred to as "Measurements"), and the ones interpolated at l_h employed in trailing-edge inserts (referred to as "Interpolation") are shown. The relative error for the original correlations stated by the

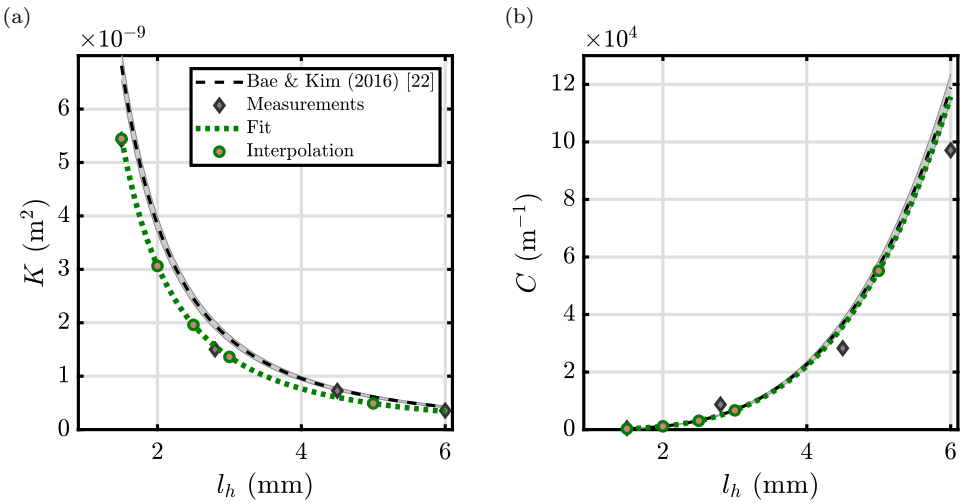

Fig. 6. Flow permeability K (a) and form coefficient C (b) as a function of the hole spacing. Measurements (diamond markers) are compared to empirical correlations (dashed line) reported in [24], together with the 3% relative error stated by the authors (grey shadowed area).

Table 2
Characteristics of permeable micro-structures measured on samples with $t = 0.01$ m. P stands for perforated and MF stands for metal foam. K and C values are interpolated from Eq. (2) (a) and (b) employing the corresponding l_h value; measured values (computed from fit of experimental data to Eq. (1)) were reported in a preliminary analysis [25], hence the small discrepancies among them. Similarly, the porosity σ is now computed with the corrected d_h of 754 µm to account for D-shaped holes.

Type	d_c (mm)	d_h (mm)	l_h (mm)	σ (-)	K (m^2)	C (m^{-1})
P	-	0.8	1.5	0.40	54×10^{-10}	279
P	-	0.8	2	0.22	31×10^{-10}	1138
P	-	0.8	2.5	0.14	20×10^{-10}	3065
P	-	0.8	3	0.10	14×10^{-10}	6681
P	-	0.8	5	0.04	5×10^{-10}	55,189
MF	1.20	-	-	-	64×10^{-10}	-
MF	0.80	-	-	0.917	32×10^{-10}	2333
MF	0.58	-	-	0.905	15×10^{-10}	3939
MF	0.45	-	-	0.893	5×10^{-10}	10,335

authors (equal to 3%) is also depicted as a grey shadowed area. Results show that both correlations are in good agreement, confirming the goodness of the permeability characterization.

Finally, a summary of the characteristics of all perforated configurations created is presented in Table 2, where the resistivity $R = K/\mu$ is also reported for completeness. Since the noise scattering analysis includes a comparison with inserts manufactured with metal foams, a summary of relevant parameters previously measured [9,23] for metal foams with $d_c = 450$, 580 and 800 µm, is also included. For the metal foam with $d_c = 1200$ µm, permeability data as reported by the manufacturer is included.

2.4. Tortuosity

A preliminary comparison between metal foams and straight periodically channelled inserts [25] showed that trailing edges with diverse flow permeability and form coefficient might abate noise similarly; hence, although it is widely recognized that these two properties have a significant impact [5,11], they might not be sufficient to fully characterize the noise mitigation capabilities of structures with different pore arrangements. In the present manuscript, tortuosity τ is proposed to account for the very different micro-structure of metal foam and channeled edges. Tortuosity $\tau \equiv l_p/t$ is usually defined[1] as the ratio between the average pore length l_p to the thickness of the porous medium t [28]. From this definition, it stems that straight channels have $\tau_Y = 1$. For the metallic foams, the tortuosity of the pore phase is statistically computed with random walk models [29]. To this aim, *pytrax* [30], an open-source *Python* suite is employed on CT-scanned samples (size:

[1] Note that a distinction between tortuosity τ, as defined in the present manuscript, and tortuosity factor $\kappa = \tau^2$ should be made [26]. For more information about the physical interpretation of the latter quantity, the reader is referred to the excellent review of Tjaden et al. [27].

Table 3
Tortuosity of metal foams (void phase) computed with random walk methods.

d_c (μm)	τ_X	τ_Y	τ_Z	τ
450	1.142 ± 0.007	1.194 ± 0.007	1.141 ± 0.007	1.158 ± 0.004
580	1.115 ± 0.006	1.153 ± 0.007	1.143 ± 0.006	1.137 ± 0.004
800	1.107 ± 0.006	1.129 ± 0.006	1.113 ± 0.006	1.116 ± 0.003
1200	1.079	1.061	1.088	1.076

10 × 10 × 5 mm^3; resolution: 12 μm) of metal foams with d_c = 450, 580 and 800 μm. Random walk processes mimic the diffusion process of non-sorbing particles, i.e. walkers, randomly distributed within porous media [31]. The algorithm begins a time sequence in which each walker randomly selects a neighbouring voxel; if the chosen voxel is also void, the walker then migrates to that position; if not, the walker does not move at that time-step [27]. The mean squared displacement of the ensemble of random walkers $\overline{r(t)^2}$ is then computed as

$$\overline{r(t)^2} = \frac{1}{n_w}\sum_{i=1}^{n_w}\left(r_{X,i}(t)^2 + r_{Y,i}(t)^2 + r_{Z,i}(t)^2\right) \tag{3}$$

where n_w is the total number of walkers, and $r_{X,i}$, $r_{Y,i}$ and $r_{Z,i}$ refer to the displacement of the walker i along X, Y and Z respectively. The mean squared displacement within porous media $\overline{r(t)^2}_p$ is then lower than the one obtained in a fully void space $\overline{r(t)^2}_v$. The degree of reduction, i.e. τ, is then computed as [32]

$$\tau = \sqrt{\frac{\overline{\dot{r}^2}_v}{\overline{\dot{r}^2}_p}} \tag{4}$$

where $\dot{r}$ refers to the time derivative of r. An accurate computation of τ is dependant on both the number of walkers and time-steps n_t. To obtain reliable τ values, 50,000 walkers and 50,000 time-steps are employed after performing a parametric study. From Eq. (3), it can be inferred that considering only axial mean square displacements, the tortuosity in a specific direction (τ_X, τ_Y, τ_Z) can be also computed. Results, presented in Table 3, are obtained from an ensemble of 100 simulations; reported values correspond to the ensemble average, and the uncertainty is calculated employing a 95% confidence level. From the results, it stems that metal foams are not perfectly homogeneous. To limit the uncertainty on the aeroacoustic analysis derived from using materials with somewhat heterogeneous properties, the same batch of foam material was used for the tortuosity computation and the insert construction. Similarly, the permeability characterization is carried out in such a way that $K \equiv K_Y$ and $C \equiv C_Y$.

The tortuosity values of Table 3 are in line with those previously reported in the literature [33–35] for open-cell metal foams with similar characteristics. Finally, due to the lack of availability of a CT-scan sample for the metal foam with d_c = 1200 μm, its tortuosity is obtained by extrapolating linearly metal foam data based on the cell diameter.

2.5. Open-jet correction for angle of attack

Experiments are performed at geometric angles of attack of 0 and 8 degrees. However, the open-jet configuration of the experimental set-up decreases the effective angle of attack α. For this reason, α is computed by analysing the measured pressure distribution along the chord. Static pressure measurements are obtained through 15 differential pressure Honeywell TruStability transducers (range: ± 2.5 kPa; accuracy: 12.5 Pa), connected to 30 pressure taps (with diameter of 0.4 mm). Taps are distributed within X/c = -0.99 to -0.34 along a plane inclined 15 degrees and with an offset of 20 mm with respect to the midspan plane (Fig. 1(a–c)). This feature prevents flow interference between consecutive holes.

Pressure data are sampled for 15 s at a sampling rate of 50 Hz. α is determined by comparing the static pressure distribution for the reference case against XFOIL data [18], which yields results for an airfoil in free-air conditions. The pressure coefficient, defined as $C_p = (P - P_\infty)/(0.5\rho U_\infty^2)$, is plotted as a function of the chordwise position in Fig. 7 for a wind tunnel angle of attack of 8 degrees; for the present experiments, the effective angles of attack α are 0.2 and 5.4 degrees respectively. Additionally, the suction peak close to the leading edge confirms that blockage effects are negligible [36], as expected from the low ratio of airfoil thickness to jet width (equal to 0.05). In Fig. 7, the C_p distributions obtained for perforated inserts with l_h ranging from 1.5 to 5 mm are also plotted. No significant differences between data measured for solid or any of the permeable inserts are observed; the previously reported [14,37–39] loss of lift must be therefore restricted to the contribution produced by the solid extent that is replaced by permeable material. For the current experimental set-up, that contribution amounts to only 4% of the overall lift.

2.6. Acoustic measurements

Far-field acoustic measurements are performed with a phased microphone array containing 64 G.R.A.S. 40 pH free-field microphones (frequency response: ± 1 dB; frequency range: 10 Hz to 20 kHz; max. output: 135 dB ref. 20 μPa; nominal

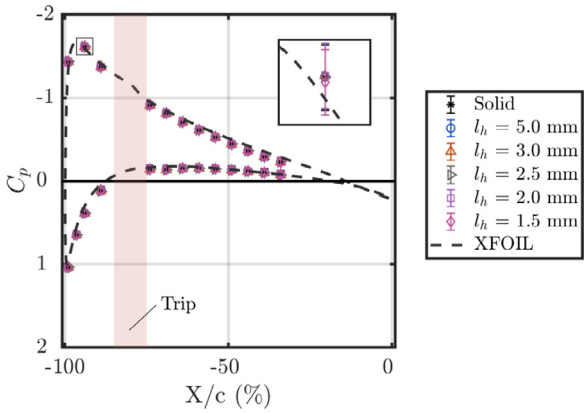

Fig. 7. Pressure coefficient C_p along the chord of the airfoil for solid and perforated inserts at a wind tunnel angle of attack of 8 degrees. XFOIL data are obtained for an angle of attack of 5.4 degrees.

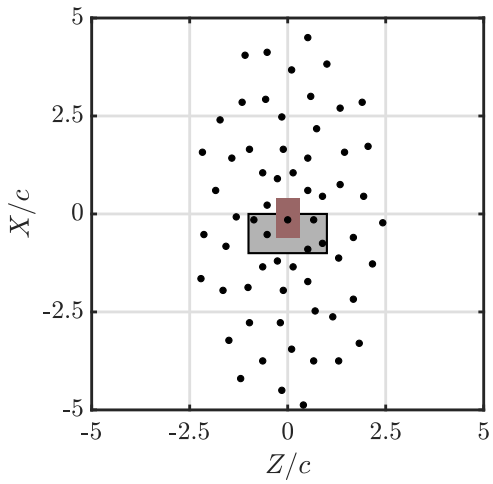

Fig. 8. Microphone distribution within the array (as seen from the back). The airfoil is marked by the grey area. The distance between trailing edge and microphone array plane is 1.01 m. The trailing edge is approximately 30 mm downstream the center microphone. The integration area is shadowed in red. Flow goes from bottom to top. (For interpretation of the references to colour in this figure legend, the reader is referred to the web version of this article.)

phase spreading: ± 3 deg.) with integrated CCP preamplifiers. The microphone distribution within the antenna, shown in Fig. 8, is optimized to reduce both the Main Lobe Width and the Maximum Sidelobe Level [40]. The spanwise and streamwise diameters of the array are 1 m and 2 m respectively (Fig. 8). The distance from the array plane to the airfoil trailing edge d is 1.01 m. The center of the array is 30 mm below the center of the airfoil trailing edge.

Data are sampled for 20 s at a sampling rate of 50 kHz. Acoustic data are divided in time blocks of 5000 samples (Δt = 0.1 s), thus resulting in a frequency resolution of 10 Hz, and windowed using a Hanning weighting function with 50% overlap. The Cross Spectral Matrix of the measured acoustic pressure is obtained by averaging spectra computed for each sample block [41]. The refraction of sound waves within the shear layer of the jet is corrected using the method proposed by Sijtsma [42]. Conventional frequency domain beamforming [43,44] is performed on a square grid ranging between $-2 < X/c < 2$ and $-2 < Z/c < 2$ and distance between grid points of 10 mm. In order to minimize the effect of extraneous noise sources, integration of the source map within $-0.3 < Z/c < 0.3$ and $-0.6 < X/c < 0.4$ (red area in Fig. 8) is performed. A more detailed parametric study on the effects of varying the spanwise and chordwise extent of the integration region on the retrieved sound levels can be found in Merino-Martínez et al. [45]. Acoustic spectra include data from 400 Hz, which corresponds to the low-frequency bound for the anechoicity of the testing chamber. The frequency high-bound depends on the free-stream velocity, and is determined by the presence of the characteristic line source at the trailing edge within beamforming maps (Fig. 9(a–f)); specifically, data up to 1.4 and 3.8 kHz are reported for measurements at free-stream velocities of 12.5 and 34 m/s respectively. The aforedescribed acoustic data reduction is often employed in trailing-edge noise research, with satisfactory results [46]. Uncertainty is estimated in ± 1 dB based on a previously reported comparison with synthetic data [47].

Beamforming results are included in Sections 3.1, 3.2 and 3.4. Yet, given the low-frequency nature (below 400 Hz) of the fundamental tones described in Section 3.5, the resolution of the array is too low to distinguish trailing-edge noise

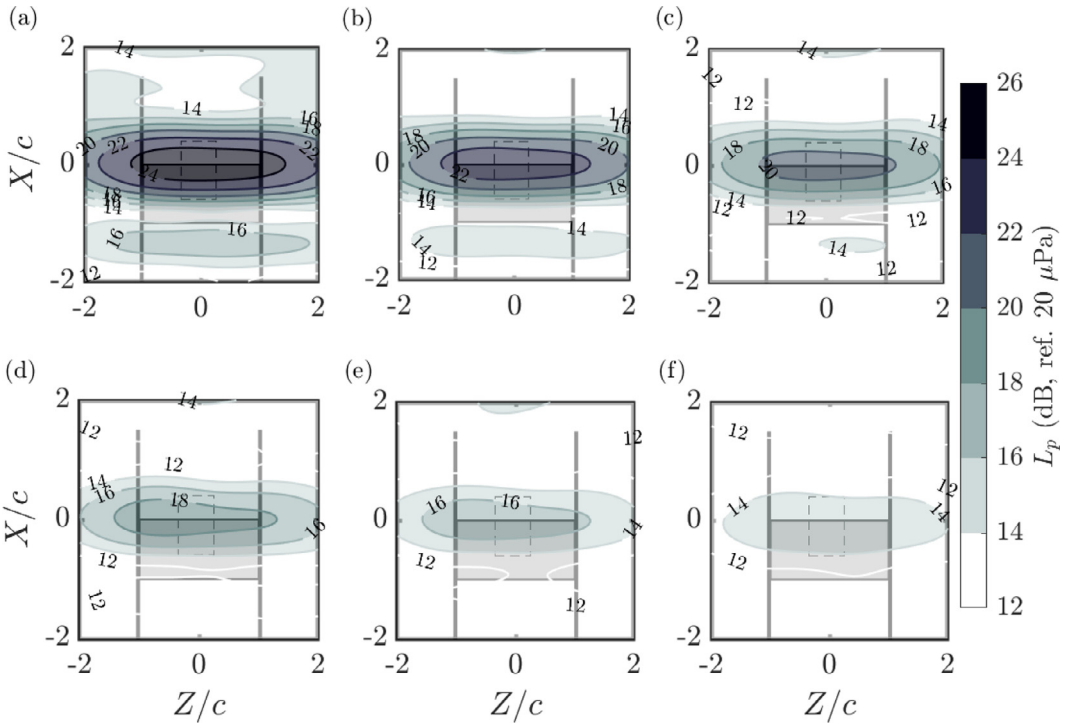

Fig. 9. Acoustic source maps measured at $U_\infty = 25$ m/s for solid and permeable trailing edges described in Section 2.2. Source maps correspond to a frequency of 1400 Hz. Integration area is marked by the dashed line. Dynamic range is 14 dB. Permeable inserts cover 20% of the chord length. (a) Solid. (b) $l_h = 5$ mm. (c) $l_h = 3$ mm. (d) $l_h = 2.5$ mm. (e) $l_h = 2$ mm. (f) l_h =1.5 mm.

from other noise sources. For this reason, far-field acoustic spectra are obtained by averaging spectra acquired by the 64 microphones [48]. To accurately resolve tones, the number of samples in each sample block is increased to 65536, thus yielding a frequency resolution of 0.76 Hz. Acoustic data corrupted by tones also present in background noise measurements are removed from spectra and replaced by linear interpolation based on adjacent points. Noise levels are not corrected for sound wave reflections; therefore their magnitude is not analysed.

3. Results

3.1. Scaling laws for noise mitigation

In Fig. 10(a), far-field acoustic spectra for a free-stream velocity $U_\infty = 20$ m/s and $\alpha = 0.2$ degrees are shown. Data are presented in terms of Sound Pressure Level in one-third octave bands $L_{p(1/3)}$ (reference pressure: $p_{\text{ref}} = 20\mu$Pa) as a function of the chord-based Strouhal number $\text{St}_c = fc/U_\infty$. Relative levels $\Delta L_{p\,(1/3)} = L_{p(1/3),\,\text{solid}} - L_{p(1/3),\,\text{permeable}}$ with respect to the baseline configuration are shown in Fig. 10(b), where positive values refer to noise abatement with respect to the fully solid airfoil. Similarly to other flow permeable structures with a more complex pore arrangement, such as foams [11], sintered granulates [10] or felts [5,14], perforated inserts yield low-frequency noise attenuation, with higher noise abatement being measured for inserts with higher flow permeability. Specifically, the largest noise attenuation (equal to 11 dB) is reported for the most permeable insert ($l_h = 1.5$ mm) at $\text{St}_c = 6.3$. Also in line with other studies [11], acoustic spectra for permeable trailing edges show cross-over Strouhal numbers St_c^*, which set the high-frequency bound for noise mitigation. St_c^* depends on the type of insert[2] Specifically, a higher St_c^* is computed for perforated inserts with higher permeability, i.e. increasing the permeability of the trailing edge not only yields higher abatement but also extends the frequency range at which noise mitigation is observed. Contrarily, a decrease in St_c^* with increasing pore size, hence permeability, has been previously reported for porous edges [9,11] (note that for foams these two properties are usually linked). This finding suggests that different mechanisms are responsible for excess noise in porous and perforated edges. This aspect will be further investigated later in this section.

In Fig. 11(a) and (b), far-field acoustic spectra for a free-stream velocity $U_\infty = 20$ m/s and $\alpha = 5.4$ degrees are shown. Similarly to data for lower lift conditions (Fig. 10(a) and (b)), perforated trailing edges with higher permeability yield higher noise mitigation below St_c^*. Main differences with respect to the previous configuration concern a decrease of the highest

[2] Note that for the design with $l_h = 1.5$ mm, St_c^* is outside the measured frequency range.

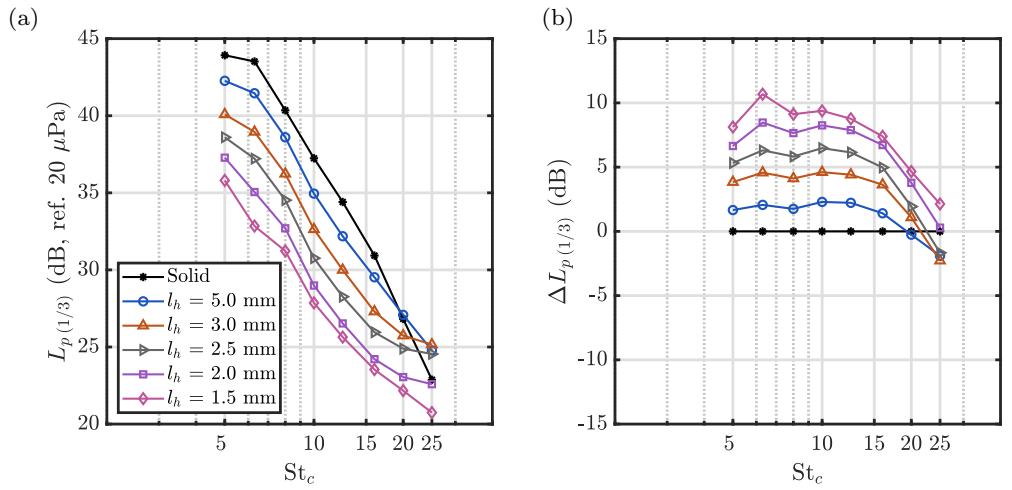

Fig. 10. Far-field acoustic spectra for the perforated inserts (with $s/c = 0.2$) at $U_\infty = 20$ m/s and $\alpha = 0.2$ degrees. (a) Absolute levels. (b) Relative levels with respect to the baseline configuration $\Delta L_{p(1/3)} = L_{p(1/3),\,\text{solid}} - L_{p(1/3),\,\text{permeable}}$.

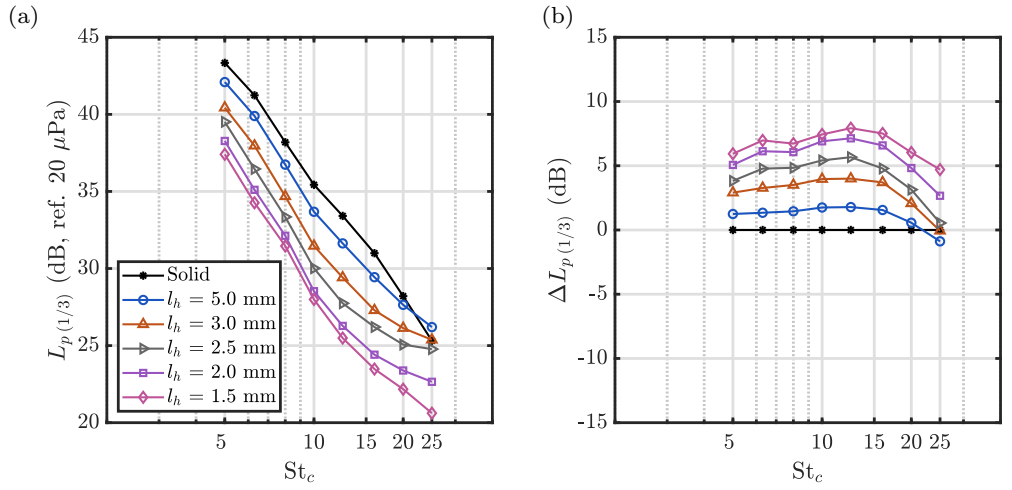

Fig. 11. Far-field acoustic spectra for the perforated inserts (with $s/c = 0.2$) at $U_\infty = 20$ m/s and $\alpha = 5.4$ degrees. (a) Absolute levels. (b) Relative levels with respect to the baseline configuration $\Delta L_{p(1/3)} = L_{p(1/3),\,\text{solid}} - L_{p(1/3),\,\text{permeable}}$.

noise abatement (for instance, the most permeable insert now yields $\Delta L_{p,(1/3)} = 8$ dB at $\text{St}_c = 12.5$) and an overall increase of St_c^*.

In Fig. 12(a), narrow-band noise attenuation ΔL_p for U_∞ of 12.5, 15, 20, 25, 30 and 34 m/s are plotted as a function of f. Only data corresponding to inserts with $l_h = 2$, 3 and 5 mm are shown for the sake of clarity. For the same reason, only one every ten points are depicted ($\Delta f = 100$ Hz). As seen in Fig. 12(b), ΔL_p data measured for different free-stream velocities collapse when plotted as a function of St_c; for ΔL_p, the relationship between frequency and U_∞ is thus linear[3]. After collapsing, data for inserts with different flow permeabilities yield curves that define the noise attenuation performance of each design independently of U_∞. In line with results presented above, characteristic curves for inserts with higher permeability allow for higher maximum noise attenuation and St_c^*. This finding allows to predict the frequency for maximum noise attenuation, or the frequency range for noise reduction for different velocities. Although not shown here for the sake of brevity, the same methodology yields a satisfactory collapse of data measured at $\alpha = 5.4$ degrees. For completeness, these characteristic curves have been compared to noise mitigation data predicted by the lower error symbolic regression models described in Sarradj and Geyer [49]. However, the overall agreement is not satisfactory; there is no collapse of predicted noise mitigation data with St_c, and higher noise mitigation maxima are predicted for materials with decreasing permeability, contrarily to experimental data presented in this manuscript.

[3] For the current analysis, the chord is used as length scale for convenience. An attempt to further collapse data for different inserts using length scales derived from the properties of the material ($\sqrt{K}$, $1/C$, $F = KC$) is presented in Appendix A

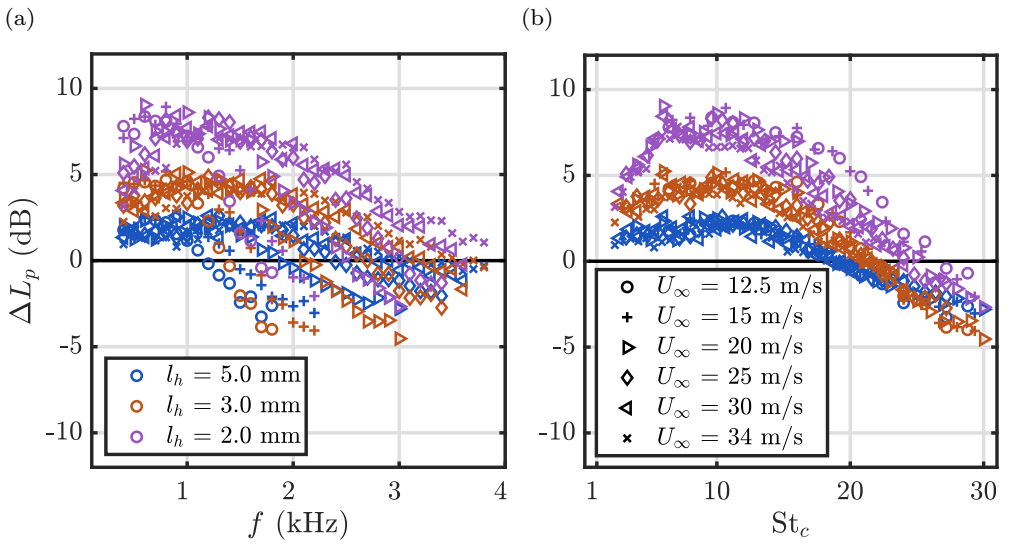

Fig. 12. Collapse of noise attenuation $\Delta L_p = L_{p,\,\mathrm{solid}} - L_{p,\,\mathrm{permeable}}$ for free-stream speeds ranging between 12.5 and 34 m/s and $\alpha = 0.2$ degrees for inserts with $l_h = 2$, 3 and 5 mm and $s/c = 0.2$. (a) ΔL_p as a function of f. (b) ΔL_p as a function of St_c.

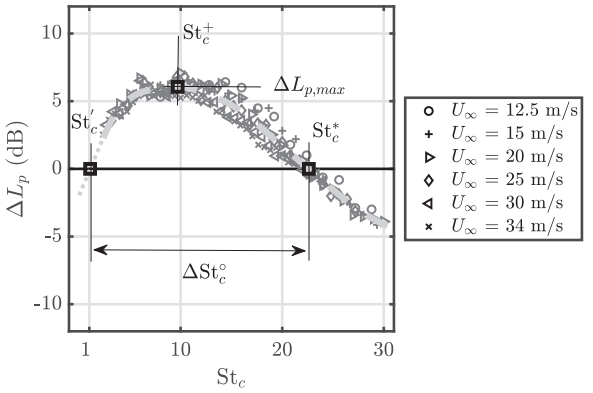

Fig. 13. Sketch depicting collapsed $\Delta L_p = L_{p,\,\mathrm{solid}} - L_{p,\,\mathrm{permeable}}$ data for the insert with $l_h = 2.5$ mm at $\alpha = 0.2$ degrees and free-stream speeds ranging from 12.5 to 34 m/s. The B-Spline fitted to experimental data is shown as a thick dashed line. In the sketch, low and high-bound cross-over Strouhal numbers St_c' and St_c^*, the Strouhal number range for noise mitigation $\Delta \mathrm{St}^\circ = \mathrm{St}_c^*$-$\mathrm{St}_c'$, the maximum noise attenuation $\Delta L_{p,\mathrm{max}}$ and its chord-based Strouhal number St_c^+ are also depicted. The thin dotted line indicates extrapolated data.

The characteristic curves shown above allow to study the change of relevant noise mitigation properties with the trailing edge permeability. Specifically, low St_c' and high-bound St_c^* cross-over Strouhal numbers, the Strouhal number range for noise mitigation $\Delta \mathrm{St}_c^\circ = \mathrm{St}_c^*$-$\mathrm{St}_c'$, the maximum noise mitigation $\Delta L_{p,\mathrm{max}}$ and the Strouhal number at which occurs St_c^+, as defined in Fig. 13, are analysed in the following. To compute these properties, cubic B-splines [50] with 8 knots and C2 continuity [51] are fitted to experimental data. In the test cases where St_c' or St_c^* are not present within the measured St_c range, the spline is extended with constant slope, as shown in Fig. 13(thin dotted line).

Firstly, the change in maximum noise attenuation $\Delta L_{p,\mathrm{max}}$ with permeability K, shown in Fig. 14(a), is analysed. $\Delta L_{p,\mathrm{max}}$ data for metal foam edges, which also collapse with St_c are also presented for comparison. To facilitate the interpretation of results, $\Delta L_{p,\mathrm{max}}$ data are fitted[4] with a hyperbolic tangent function, as defined in Eq. (5)

$$\Delta L_{p,\mathrm{max}} = \gamma_1 \tanh(\gamma_2 K) \tag{5}$$

where γ_1 defines the asymptotic $\Delta L_{p,\mathrm{max}}$ value and γ_2 the slope of the function within the low permeability range. The reasons to choose this function are twofold: firstly, it adequately mimics the asymptotic character of experimental data for increasing permeability of the edges; secondly, it passes through the point $K = 0$ m^2, $\Delta L_{p,\mathrm{max}} = 0$ dB, properly describing baseline data. These curves yield valuable information on the type of microstructure that maximizes noise mitigation. It is observed that, for perforated inserts at $\alpha = 0.2$ degrees, increasing the permeability to 3.5×10^{-9} m^2 causes up to

[4] Coefficients for the fitting of experimental data to Eq. (5) are presented in Appendix B

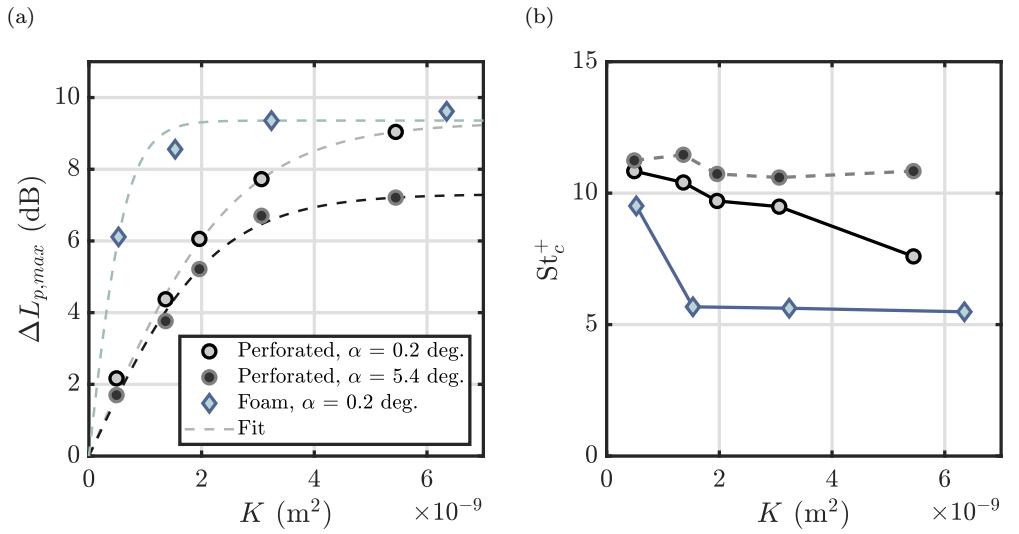

Fig. 14. Change in maximum noise mitigation with permeability for perforated and metal foam inserts at $\alpha = 0.2$ and 5.4 degrees. (a) $\Delta L_{p,\max}$. (b) St_c^+.

8.3 dB noise mitigation. Further increasing the permeability of the insert brings few additional noise attenuation benefits (approximately 1 dB more, up to an asymptotic value of 9.3 dB at $K = 6 \times 10^{-9}$ m^2). Furthermore, increasing α to 5.4 degrees penalizes noise mitigation: $\Delta L_{p,\max}$ values measured at a higher-lift condition are lower than those computed at 0.2 degrees independently of the permeability. Interestingly, lower-permeability variants are less sensitive to a change in α: for instance, for the least permeable perforated insert ($l_h = 5$ mm) increasing α yields a $\Delta L_{p,\max}$ loss equal to 0.5 dB, whilst for the most permeable insert ($l_h = 1.5$ mm) the decrease is equal to 2 dB. Given the lift decrease and drag increase when employing inserts with higher permeability [5,38], as well as their higher sensitivity to changes in α, the employment of perforated inserts with moderate flow permeability (below a threshold of $K = 3.5 \times 10^{-9}$ m^2) is recommended. For inserts manufactured with metal foams, similar features are found: maximum noise attenuation increases rapidly with permeability up to approximately 8.4 dB (for a K threshold of 1×10^{-9} m^2, less than one third of the value reported for perforated pores); further increasing K only yields a 1 dB gain in $\Delta L_{p,\max}$, up to a maximum noise mitigation of 9.4 dB. Both metal foam and perforated trailing edges share a high bound for $\Delta L_{p,\max}$ of 9.3–9.4 dB; yet, for a given K (below 6×10^{-9} m^2) an additional increase of up to 4 dB (for edges with K between 0.5 and 2×10^{-9} m^2) can be achieved by employing a random pore arrangement. Similarly, to obtain similar $\Delta L_{p,\max}$ levels, perforated inserts must be more permeable than metal foam trailing edges. In view of these findings, the permeability of the trailing edge can be therefore considered as a good indicator for noise mitigation effectiveness, but it is insufficient to fully characterize the noise scattering of trailing edges with significant micro structural differences. Other parameters describing the different pore organization of permeable materials, such as tortuosity, need to be considered to fully characterize their noise scattering. This analysis will be presented in Section 3.2.

In Fig. 14(b), the chord-based Strouhal number at which $\Delta L_{p,\max}$ occurs, St_c^+, is shown for perforated inserts at $\alpha = 0.2$ and 5.4 degrees, and metal foam inserts at $\alpha = 0.2$ degrees as a function of K. For perforated inserts at $\alpha = 0.2$ degrees, an approximately linear decrease of St_c^+ with K is measured: the least permeable insert produces maximum noise attenuation at $\mathrm{St}_c^+ = 11$, while the most permeable insert yields $\mathrm{St}_c^+ = 7.5$. Therefore, perforated trailing edges with increasing permeability not only yield higher $\Delta L_{p,\max}$ but also mitigate low-frequency noise more efficiently. Increasing the angle of attack to $\alpha = 5.4$ degrees leads to a constant St_c^+ value of 11 for all K; similarly to $\Delta L_{p,\max}$, inserts with higher flow permeability are more sensitive to a change in α. Regarding metal foams, low-permeability inserts ($K = 0.5 \times 10^{-9}$ m^2) yield maximum noise attenuation at $\mathrm{St}_c^+ = 9.5$, close to the value for perforated edges. However, increasing K to 1.5×10^{-9} m^2 rapidly brings St_c^+ to 5.7; for higher flow permeability St_c^+ is approximately constant. Therefore, the choice of an adequate pore arrangement allows not only to obtain different maximum noise attenuation levels (below a certain K threshold), but also to target specific frequencies.

In Fig. 15, the lower-bound cross-over Strouhal numbers $\mathrm{St}_c^{'}$, computed for perforated and metal foam inserts at $\alpha = 0.2$ and 5.4 degrees, are plotted as a function of K. For perforated inserts at $\alpha = 0.2$ degrees, $\mathrm{St}_c^{'}$ increases from 0.04 to 2.44 within the measured permeability range. Increasing the angle of attack, or employing inserts with random pore distribution (i.e. metal foams) yield higher $\mathrm{St}_c^{'}$; specifically, $\mathrm{St}_c^{'}$ values between 0.96 and 2.68 are measured for the former case, and between 2.28 and 2.96 for the latter. It can be therefore concluded that to guarantee noise mitigation within the very low frequency range one must employ edges with low permeability and ordered pore arrangement.

In Fig. 16(a), high-bound cross-over Strouhal number St_c^* data are presented. For this quantity, a linear-like increase of St_c^* with K is measured for perforated inserts at $\alpha = 0.2$ degrees. Therefore, besides higher noise attenuation, inserts

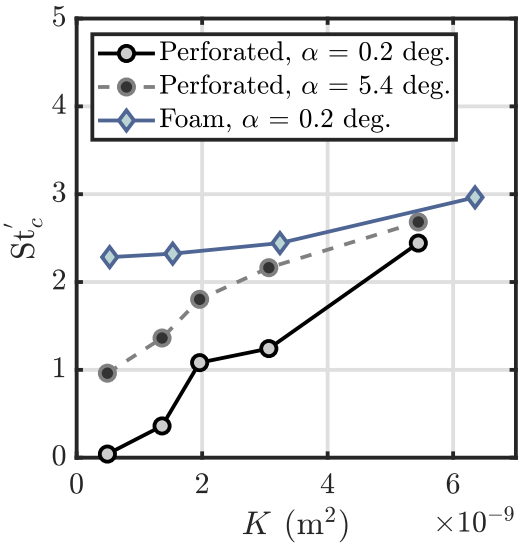

Fig. 15. Change in St_c' with permeability for perforated and metal foam inserts at $\alpha = 0.2$ and 5.4 degrees.

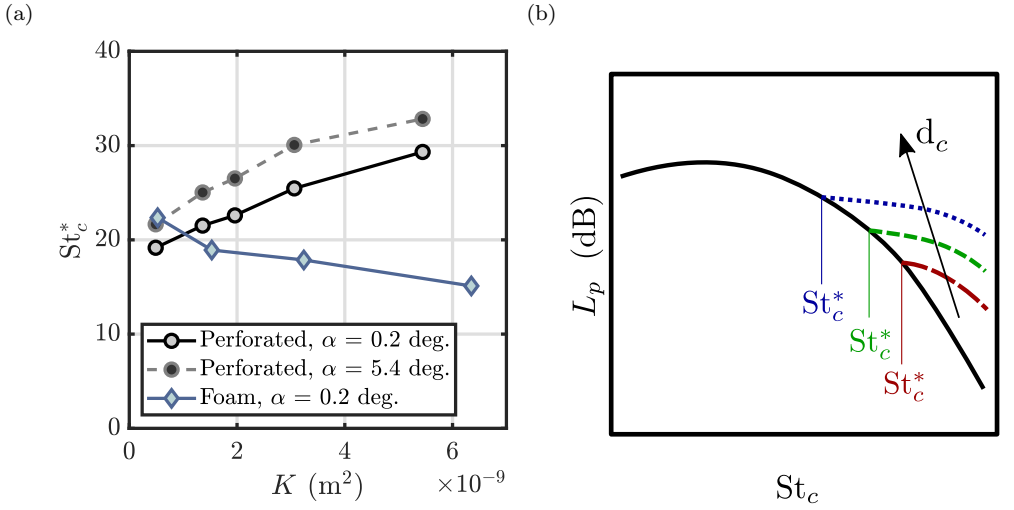

Fig. 16. (a) Change in St_c^* with permeability for perforated and metal foam inserts at $\alpha = 0.2$ and 5.4 degrees. (b) Sketch depicting typical roughness noise features for porous edges. Black line represents baseline (smooth surface) trailing-edge noise. Dashed lines illustrate roughness noise contributions for increasing pore size d_c, i.e. higher roughness.

with higher permeability also mitigate noise up to higher frequencies (in line with results shown in Fig. 10(a) and (b)). Additionally, increasing the angle of attack to $\alpha = 5.4$ degrees further increments St_c^*. For metal foams, a different trend is reported: a lower St_c^* is measured for increasing permeability of the insert. The opposite trends for the variation of St_c^* with K indicate that different mechanisms are responsible for high-frequency noise in perforated and metal foam edges. For metal foam edges, high-frequency excess noise is caused by surface roughness [9,11]; it has been previously shown that a larger pore size, that often translates in larger K, generates higher noise and becomes more relevant at lower frequencies [52], in agreement with results in Fig. 16(b). It is also important to remark that, for the present data-set, narrowband contributions are only found for the most permeable perforated insert; however, the low-frequency nature of these tones suggests that they are not driven by roughness. Their nature will be addressed in detail in Section 3.5.

The resulting St_c range for noise abatement $\Delta\mathrm{St}^\circ = \mathrm{St}_c^*$-$\mathrm{St}_c'$, measured for perforated and metal foam inserts at angles of attack of 0.2 and 5.4 degrees, is shown in Fig. 17. Results are similar to those found for St_c^*, i.e., perforated edges with higher permeability yield acoustic benefits within a wider frequency range, and increasing α further extends it (approximately an increase of $\Delta\mathrm{St}^\circ = 4$ with α is measured independently of K). For metal foam edges, a decrease in $\Delta\mathrm{St}^\circ$ with K is observed instead; hence, contrarily to perforated edges, more permeable metal foam edges yield noise mitigation within a smaller frequency range. The similarity between Fig. 16(a) and Fig. 17 suggests that $\Delta\mathrm{St}^\circ$ is particularly sensitive to the appearance of noise generation mechanisms other than edge noise, that generate high-frequency excess noise.

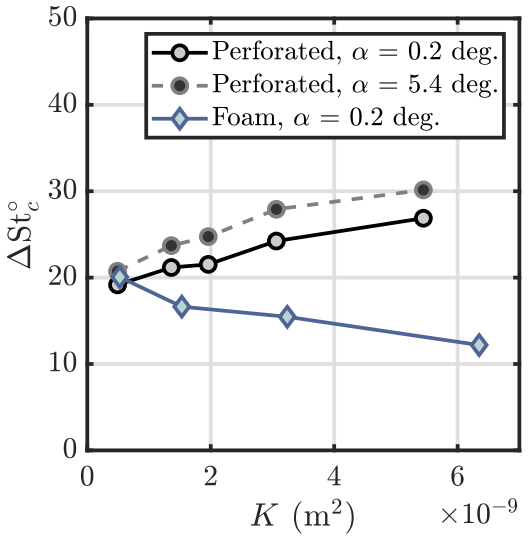

Fig. 17. Change in $\Delta \mathrm{St}_c^\circ$ with permeability for perforated and metal foam inserts at $\alpha = 0.2$ and 5.4 degrees.

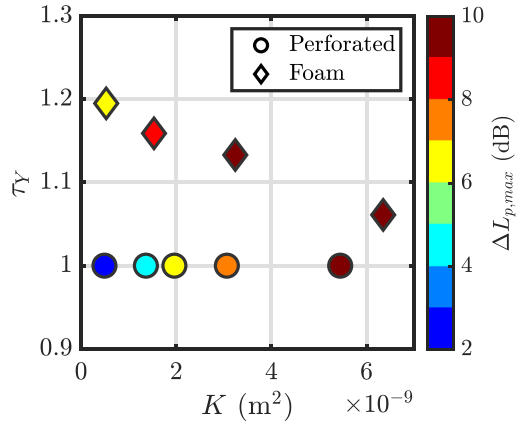

Fig. 18. Maximum noise attenuation $\Delta L_{p,\max}$ as a function of K and τ_Y for $\alpha = 0.2$ deg.

3.2. Effect of tortuosity on noise mitigation

Following the discussion in Section 3.1, tortuosity τ_Y is proposed, in addition to K, as an additional indicator for the noise mitigation capabilities of permeable trailing edges. In Fig. 18, $\Delta L_{p,\max}$ data are plotted as a function of flow permeability and tortuosity for perforated and metal foam trailing edges.

It is observed that, for a given permeability, micro-structures with more tortuous pore paths, i.e. foams, gain up to 4 dB noise attenuation with respect to straight channelled inserts. To this end, highly tortuous pore arrangements, such as those derived from sintering [53] or casting around space-holders [54] manufacturing processes, might yield additional benefits for low-noise applications. For the current experimental set-up, a trailing edge with permeability of $K = 1 \times 10^{-9}$ m^2 and tortuosity $\tau_Y \simeq 1.15$ is a good trade-off between aerodynamic and broadband acoustic performance.

3.3. Scaling of far-field acoustic pressure with free-stream velocity

The exponent m for the scaling of far-field mean-squared acoustic pressure with free-stream velocity is now analysed. This quantity is computed fitting the Overall Sound Pressure Level (OSPL) [55], calculated as

$$\mathrm{OSPL} = 10 \log_{10} \sum_{f_c} 10^{L_{p(1/3)}/10\,\mathrm{dB}} \tag{6}$$

to experimental data measured at different speeds. To isolate broadband noise mitigation, only frequency bands where noise abatement with respect to the baseline configuration is measured are considered. For the same reason, the most permeable perforated ($l_h = 1.5$ mm) and metal foam ($d_c = 1200$ µm) inserts are excluded from the analysis because, as will be seen in

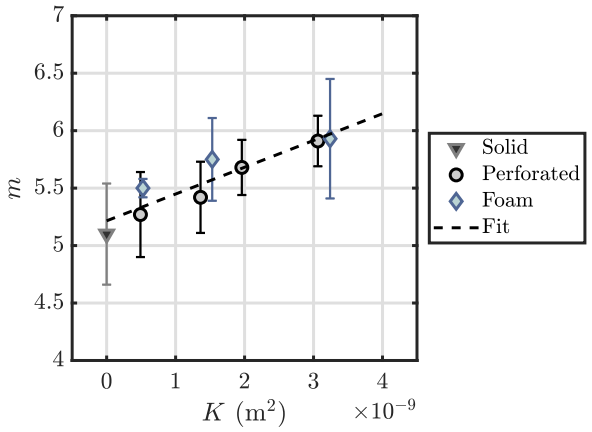

Fig. 19. Analysis of the exponent m of the scaling low of the far-field acoustic pressure with free-stream velocity U_∞. Change in m with permeability K for metal foam and perforated inserts at $\alpha = 0.2$ degrees.

Section 3.5, acoustic spectra for the former contain tones; for the latter, a low-frequency broadband hump is measured. The fit of experimental OSPL data to U_∞ is performed employing

$$\mathrm{OSPL} = m10\log_{10}\left(\frac{U_\infty}{U_{\mathrm{ref}}}\right) + \eta \tag{7}$$

with η being an additional fit coefficient and $U_{\mathrm{ref}} = 1$ m/s for convenience. For the baseline insert, the fit yields $m = 5.1$, in line with theoretical [56,57] and experimental results [58]. The computed exponent m is plotted (together with the uncertainty, estimated as the 95% confidence bounds of the fit) as a function of K in Fig. 19 for perforated and metal foam inserts at $\alpha = 0.2$ degrees. In spite of the many spectral differences described above, exponents m for micro-structures with similar flow permeability are comparable (within their uncertainty range) independently of the pore arrangement. This result suggests that although specific noise mitigation features ($\mathrm{St}_c^{'}$, St_c^{*}, $\Delta L_{p,\max}$, etc.) for permeable inserts rely on certain micro-structural properties, they all act upon noise generation through the same mechanism, i.e. decreasing the acoustic impedance jump at the surface discontinuity and creating distributed noise scattering [9]. Data for both perforated and metal foam edges increase linearly from $m = 5.1$ (at $K = 0$ m^2, solid case) to $m = 5.9$ (at $K = 3 \times 10^{-9}$ m^2). Consequently, m values are fitted[5] to a line, defined as follows

$$m = \chi_1\, K + \chi_2 \tag{8}$$

The linear increase suggests intrinsic changes in the noise source nature (from a dipole over a non-compact to a compact surface), and might be explained by a more effective distribution of noise sources along the permeable extent for increasing K, that decreases the ratio of effective chord length to noise source extension, i.e., it promotes the compactness of the airfoil.

3.4. Effect of the relative permeable chord length on noise abatement

Tests are carried out to assess the effect of a change in the permeable chordwise extent s on noise mitigation. To this aim, besides data gathered for $s/c = 0.2$ (40 mm), additional experiments are carried out for perforated inserts with $l_h = 2$ and 5 mm; specifically, these inserts are taped at both sides, leaving only $s/c = 0.1$ (20 mm) and $s/c = 0.05$ (10 mm) exposed to the flow. As seen in Figs. 20(a) and (b), noise mitigation data for varying U_∞ also collapse when non-dimensionalizing the frequency as Strouhal number, yielding the curves already described in Section 3.1. Similarly, relevant parameters such as $\mathrm{St}_c^{'}$, St_c^{*}, $\Delta\mathrm{St}^{\circ}$, $\Delta L_{p,\max}$ and St_c^{+} are computed fitting experimental data to a spline. For data corresponding to shorter permeable lengths, the lower-bound cross-over Strouhal number $\mathrm{St}_c^{'}$, is directly computed from measured data, i.e., no data extrapolation is required.

Results are shown in Fig. 21(a) and (b), where $\mathrm{St}_c^{'}$, St_c^{*}, $\Delta L_{p,\max}$ and St_c^{+} are plotted as a function of the permeable length to chord ratio s/c for perforated inserts with $l_h = 5$ and 2 mm respectively. For the perforated insert with $l_h = 5$ mm, an overall decrease in all St-based parameters for increasing s/c is found (Fig. 21(a)); hence, a longer permeable insert with this pore arrangement does not broaden the frequency range for noise abatement, but is beneficial to tackle lower frequencies. Data for the perforated insert with $l_h = 2$ mm show a decrease of $\mathrm{St}_c^{'}$ with s/c; yet, St_c^{*} has an approximately constant value of 25 for all s/c. Consequently, for this insert the noise mitigation range is extended for increasing s/c.

These findings are analysed more in detail in Fig. 22(a), where the frequency range for noise mitigation $\Delta\mathrm{St}_c^{\circ}$ is plotted as a function of s/c. For the perforated insert with $l_h = 5$ mm, increasing s/c yields few additional benefits in $\Delta\mathrm{St}_c^{\circ}$; for the one

[5] Fit coefficients are reported in Appendix B

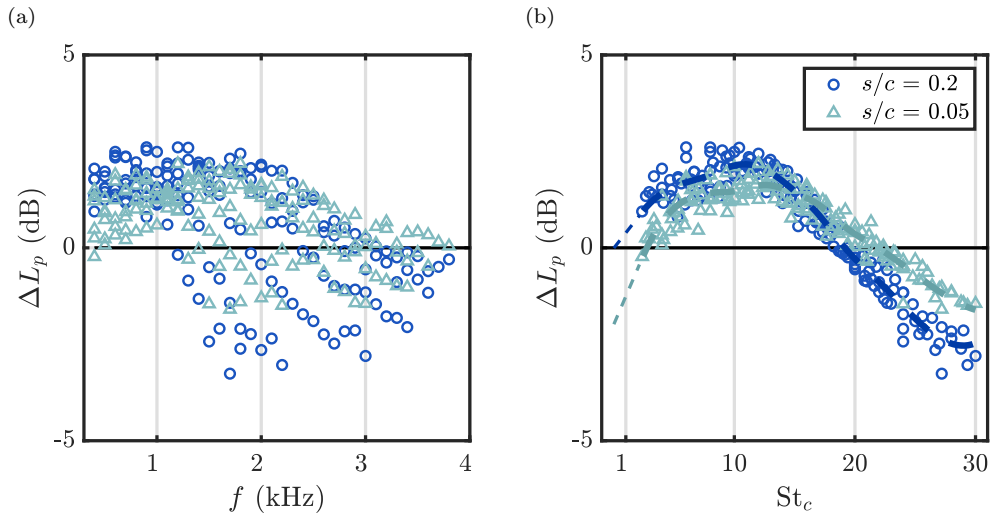

Fig. 20. Collapse of $\Delta L_p = L_{p,\,\mathrm{solid}} - L_{p,\,\mathrm{permeable}}$ with St_c for perforated inserts with $l_h = 5$ mm and permeable extent $s/c = 0.2$ and $s/c = 0.05$. Data are measured at U_∞ ranging from 12.5 to 34 m/s and $\alpha = 0.2$ degrees. Dashed lines represent the B-Spline fitted to experimental data. Thick dashed lines indicate interpolated data. Thin dashed lines indicate extrapolated values.

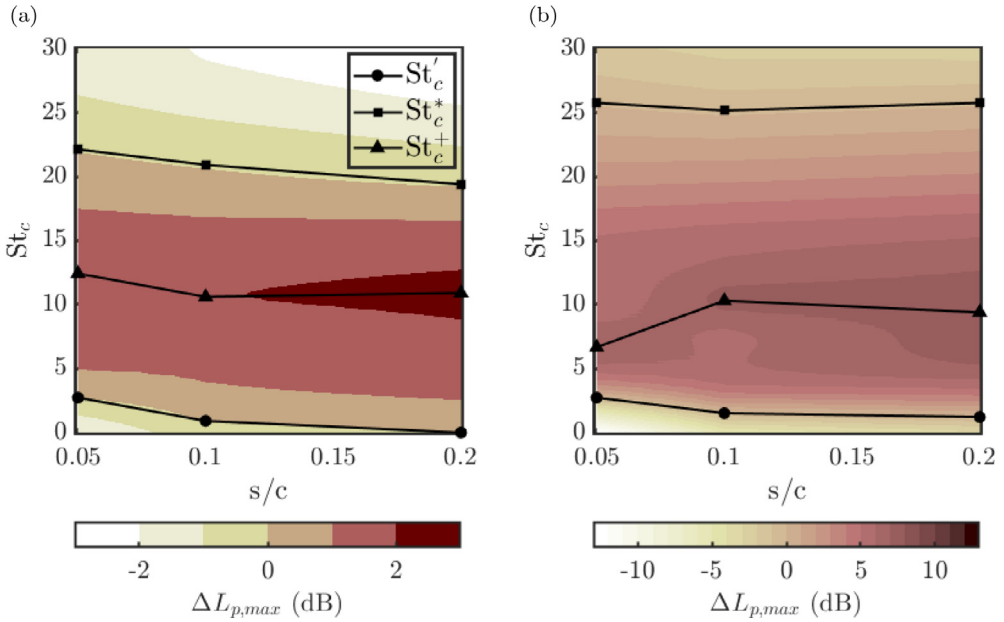

Fig. 21. Change in maximum noise attenuation $\Delta L_{p,\mathrm{max}}$ with permeable chordwise length s/c and chord-based Strouhal number St_c for perforated inserts with $l_h = 5$ (a) and 2 mm (b) at $\alpha = 0.2$ degrees.

with $l_h = 2$ mm, a slight extension of the frequency range (from 23 at $s/c = 0.05$ to 24.5 at $s/c = 0.2$) is reported instead. This result evidences that increasing s/c is not a convenient way to achieve noise mitigation throughout a wider frequency range (to this end, increasing K is more effective), but rather to enhance abatement upon lower frequencies.

Finally, maximum noise abatement $\Delta L_{p,\mathrm{max}}$ data are plotted in Fig. 22(b). As in Section 3.1, experimental data are fitted[6] with

$$\Delta L_{p,\mathrm{max}} = \xi_1 \tanh\left(\xi_2 \frac{s}{c}\right) \tag{9}$$

[6] Fitting coefficients are reported in Appendix B.

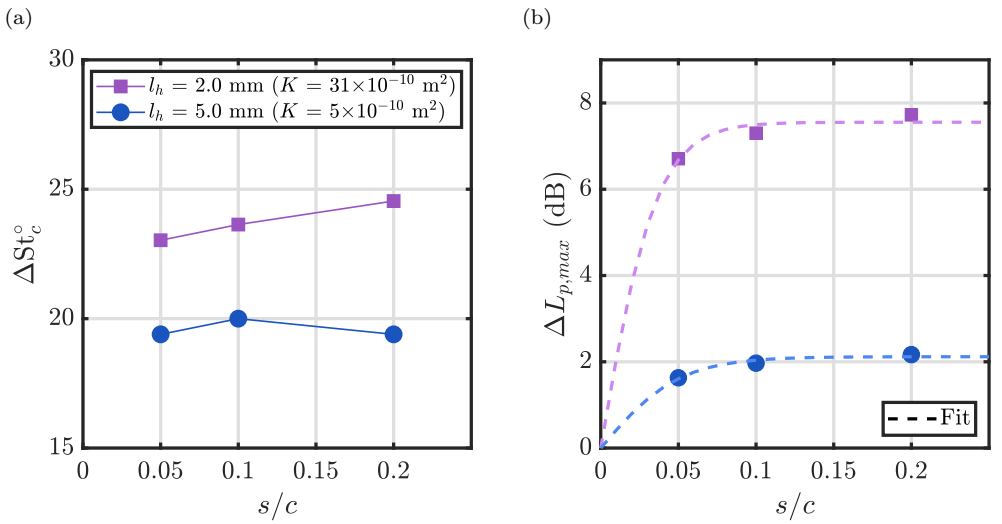

Fig. 22. Change in the frequency range for noise mitigation $\Delta \mathrm{St}_c^\circ$ (a) and maximum noise attenuation $\Delta L_{p,\max}$ (b) with permeable chordwise length s/c for perforated inserts with l_h = 2 and 5 mm (α = 0.2 deg.).

Results show that with s/c = 0.05, inserts with l_h = 2 mm and 5 mm abate up to 1.6 and 6.7 dB respectively. Further increasing s/c yields negligible additional abatement (lower than 1 dB). Since a longer permeable extent would decrease lift and increase drag, this value represents a good trade-off between noise mitigation and aerodynamic performance. It is interesting to note that for the s/c = 0.05 configuration the permeable extent approximately coincides with the boundary layer thickness at the trailing edge for the baseline configuration (previous studies [9,12] report a value of 9.3 mm at U_∞ = 20 m/s); whether this observation can be generalized or is merely a coincidence for the current experimental set-up will be addressed in future research. It is also interesting to note that some of the features derived from decreasing the length of the permeable insert, such as the decrease in $\Delta L_{p,\max}$, or the increase in St_c^*, are in line with those reported in Section 3.1 for increasing α. This might be related to the passage of steady flow through permeable media due to a pressure imbalance between pressure and suction side, illustrated, for instance, by Mößner and Radespiel [59], that decreases the effective length of the permeable extent.

3.5. Appearance of shedding-related tones

In spite of the just reported benefits regarding broadband noise mitigation, for permeable inserts with periodic arrangement of the channels and high flow permeability, an undesired tone is measured independently of the angle of attack. Specifically, such a feature is found in far-field acoustic spectra for the most permeable perforated insert (l_h = 1.5 mm). In Fig. 23, narrow band acoustic measurements for a free-stream velocity of 25 m/s and an angle of attack of 0.2 degrees are presented, together with background noise measurements and data for the l_h = 5 mm and reference configurations. A strong (+30 dB over broadband noise levels) tonal component is measured at a frequency of 208 Hz, with harmonics at 416 and 624 Hz.

In Fig. 24(a), narrow-band spectra for the l_h = 1.5 mm insert at U_∞ = 15, 20, 25, 30 and 34 m/s are shown. Only at U_∞ = 15 m/s no tones are observed within the measured frequency range. When f is scaled employing the thickness of the airfoil at the solid-permeable junction h = 15.7 mm and the free-stream velocity, all tones collapse (Fig. 24(b)). The analysis yields a fundamental tone at $\mathrm{St}_{h,1}$ = 0.13, with visible harmonics up to $\mathrm{St}_{h,i}$ = 0.52. Such values are in line with those typically found for blunt trailing-edge noise [14,58], in which a similar peak arises due to shedding from the blunt trailing edge. Therefore, the nature of this tone seems to be related to the appearance of periodic flow phenomena, i.e. vortex shedding from the apparent blunt end of the airfoil aluminium body, due to the high permeability and periodic pore arrangement of the insert. The introduction of a certain degree of randomness in the pore distribution might alter the organization and periodicity of vortices, thus preventing the appearance of strong tones. In agreement with this hypothesis, the metal foam with d_c = 1200 μm and the perforated insert with l_h = 1.5 mm have comparable flow permeability ($K \simeq 6 \times 10^{-9}$ m^2); yet, tones are solely reported for the latter insert.

This aspect is further addressed in an additional test in which the permeable insert is taped, leaving exposed to the flow a permeable chordwise extent equal to s/c = 0.1 = 20 mm. A similar analysis for this test case (Fig. 25(a) and (b)) (with a thickness h of 9.5 mm) reveals a strong peak at $\mathrm{St}_{h,1}$ = 0.10, and subsequent harmonics. Note that for this configuration, additional weaker tones appear around the fundamental one. The origin of these might be in the taping procedure: if tape is not perfectly parallel to the trailing edge, or is applied differently at suction and pressure sides, one might expect slight

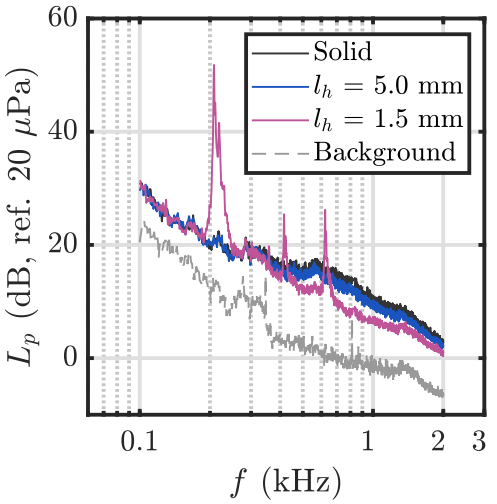

Fig. 23. Narrow band far-field acoustic spectra for the solid and perforated inserts with l_h = 5 mm and l_h = 1.5 mm at U_∞ = 25 m/s and α = 0.2 deg.

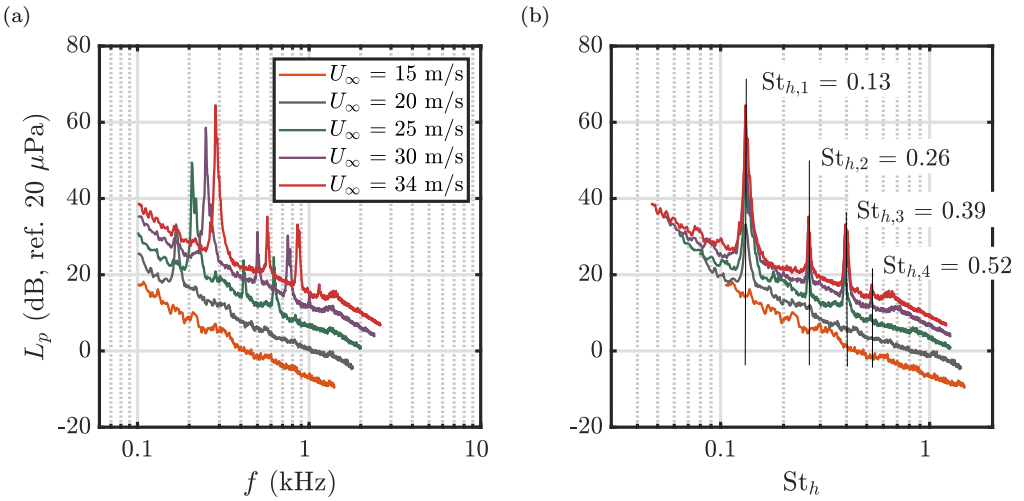

Fig. 24. Collapse of tonal noise with St_h for the perforated insert with l_h = 1.5 mm at free-stream velocities ranging from 15 to 34 m/s and α = 0.2 deg. Permeable surface extends for the last 20% of the chord (40 mm). (a) Far-field acoustic spectra as a function of f. (b) Far-field acoustic spectra as a function of St_h.

variations in the solid-permeable junction thickness along the span; hence, some deviations from the fundamental tone frequency.

Finally, in Fig. 26, both $St_{h,1}$ values are shown as a function of the thickness ratio h/δ^*. Displacement thickness data are obtained from a previous boundary layer characterization [12], performed at 20 m/s employing high-speed Particle Image Velocimetry; only data measured at this free-stream velocity are shown. Experimental data are compared to the empirical relation for $St_{h,1}$ proposed by Brooks et al. [58], defined as

$$St_{h,1} = \frac{0.212 - 0.0045\Psi}{1 + 0.235(h/\delta^*)^{-1} - 0.0132(h/\delta^*)^{-2}} \tag{10}$$

where Ψ is the solid angle (in degrees) between the sloping surfaces upstream of the trailing edge. For permeable extents s/c = 0.1 and s/c = 0.2 the solid angles Ψ are respectively 21 and 19 degrees. For comparison, data reported in the original study for a flat plate (Ψ = 0 deg.) and a NACA 0012 airfoil (Ψ = 14 deg.) are also included. A fair agreement between measured data and predictions is found independently of the permeable extent; the shedding-related nature of the tone is therefore confirmed.

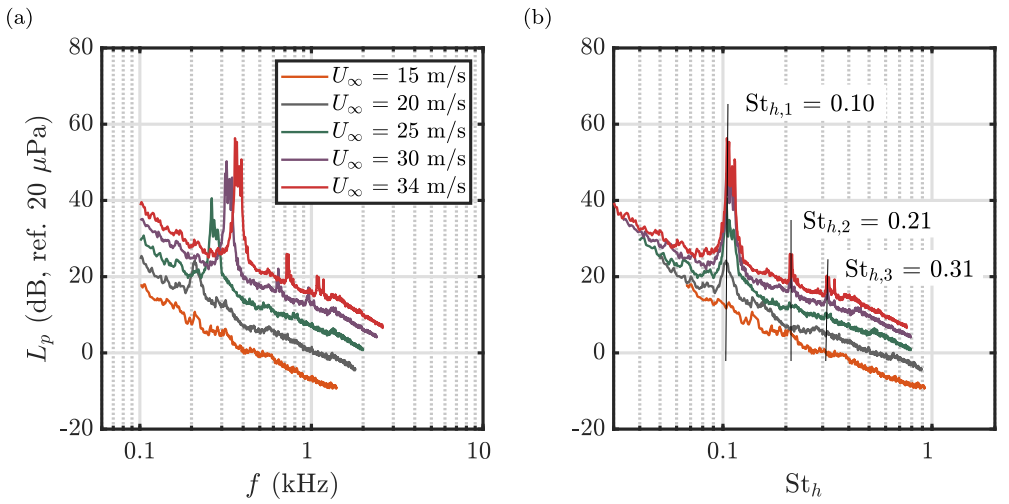

Fig. 25. Collapse of tonal noise with St_h for the perforated insert with l_h = 1.5 mm at free-stream velocities ranging from 15 to 34 m/s and α = 0.2 deg. Permeable surface extends for the last 10% of the chord (20 mm). (a) Far-field acoustic spectra as a function of f. (b) Far-field acoustic spectra as a function of St_h.

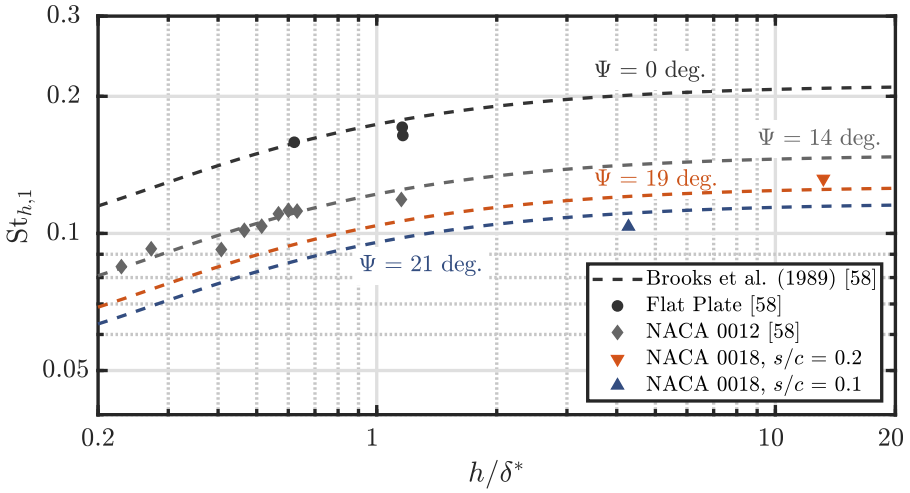

Fig. 26. Trailing-edge thickness based Strouhal number of the first peak $\mathrm{St}_{h,1}$ as a function of thickness ratio h/δ^*. The empirical prediction proposed in Brooks et al. [58] (Eq. (10)) is plotted for a flat plate (Ψ = 0 deg.), a NACA 0012 airfoil (Ψ = 14 deg.) and a NACA 0018 airfoil with s/c = 0.1 (Ψ = 21 deg.) and s/c = 0.2 (Ψ = 19 deg.). Reported $\mathrm{St}_{h,1}$ values [58] for a flat plate and a NACA 0012 airfoil are also depicted for comparison.

4. Conclusions

In this manuscript, acoustic measurements on a NACA 0018 airfoil (with chord c = 0.2 m) equipped with solid and permeable trailing-edge inserts are performed by means of a microphone antenna. To obtain criteria for maximizing noise abatement while limiting changes in aerodynamic performance, trailing edges with straight open channels that link suction and pressure sides are manufactured. For comparison, trailing-edge inserts manufactured with open-cell metal foams, with comparable flow permeability but random pore distribution, are also analysed.

Far-field noise spectra reveal the collapse of ΔL_p, defined as the difference between noise scattering from solid and permeable edges, when nondimensionalizing frequency with chord and free-stream velocity. Collapsed data produce sine-like ΔL_p curves that define the acoustic benefits of each trailing edge independently of flow speed. From this analysis, it stems that the change in maximum noise mitigation $\Delta L_{p,\max}$ with permeability K can be accurately described with a hyperbolic tangent ($\Delta L_{p,\max} = \gamma_1 \tanh(\gamma_2 K)$, where γ_1 and γ_2 are fitting coefficients), i.e. significant noise mitigation can be achieved with moderate K, but it saturates above certain K thresholds, that depend on the type of edge employed. Specifically, permeability thresholds of 3.5×10^{-9} and 1×10^{-9} m^2 are respectively obtained for perforated and metal foam inserts. The employment of edges with permeability equal to these thresholds is therefore recommended to minimize aerodynamic penalty (i.e., decrease in lift and increase in drag) due to the use of permeable materials in lifting devices, to

maximize the frequency range for noise mitigation, and to prevent an excessive downgrade of the acoustic benefits when increasing the angle of attack. Furthermore, the tortuosity of the trailing edge is proposed to account for differences in noise mitigation reported for edges with similar permeability but different pore arrangement. This manuscript also stresses that increasing the chordwise extent of the permeable region s beyond $s/c = 0.05$ (which in the current study is in line with the boundary layer thickness at the trailing edge for the baseline configuration) does not extend the frequency range for noise mitigation, nor increases its magnitude significantly. Finally, it is also confirmed that inserts with high permeability and an ordered pore arrangement produce extremely loud tones, which are caused by vortex-shedding from the blunt edge of the airfoil solid body.

Taken together, these findings suggest that a permeable trailing edge insert with permeability equal to 1×10^{-9} m^2, with a tortuosity of 1.15 (which is in turn beneficial to avoid tones) and with $s/c = 0.05$ yields the best trade-off between broadband noise mitigation and aerodynamic loss. Future work will address optimal trailing-edge properties for more realistic conditions, i.e., cambered airfoils with longer chord, as well as the definition of the micro-structural and fluid features necessary to prevent shedding from permeable edges.

Declaration of Competing Interest

The authors declare that they have no known competing financial interests or personal relationships that could have appeared to influence the work reported in this paper.

CRediT authorship contribution statement

Alejandro Rubio Carpio: Conceptualization, Methodology, Data curation, Writing - original draft. **Francesco Avallone:** Conceptualization, Supervision, Methodology, Writing - review & editing. **Daniele Ragni:** Conceptualization, Methodology, Supervision, Writing - review & editing. **Mirjam Snellen:** Supervision, Methodology, Writing - review & editing. **Sybrand van der Zwaag:** Supervision, Methodology, Writing - review & editing.

Acknowledgments

The authors would like to acknowledge Lourenco Lima Pereira for his assistance during the characterization of the inflow conditions and Frank Schilder for his advice and feedback for the manufacturing of the inserts.

Appendix A. Additional Scaling Laws

In Section 3.1, the collapse of noise mitigation data for different free-stream velocities when plotted as a function of St_c is shown. In the analysis, the chord of the airfoil is employed as length scale for the sake of simplicity. However, an attempt to collapse data for different permeable inserts employing length scales based on hydraulic properties, such as $\sqrt{K}$, $1/C$ or $F = KC$ was also performed.

Results are shown in Figs. A.1(a), (b) and (c), where cross-over Strouhal numbers based on these quantities $St^*_{\sqrt{K}}$, $St^*_{1/C}$ and St^*_F are respectively depicted as a function of the corresponding hydraulic property for perforated and metal foam inserts at $\alpha = 0.2$ and 5.4 degrees. As seen in these plots, employing hydraulic properties does not remove the dependency of St^* on these quantities neither for perforated nor metal foam inserts. Yet, for all three properties the relation seems to be linear. Interestingly, for the collapse with $1/C$ as length scale, all data seem to collapse in a line independently of hole arrangement or lifting condition.

Similar phenomena are found for the analysis of the Strouhal number for maximum noise attenuation St^+. In Figs. A.2(a), (b) and (c), $St^+_{\sqrt{K}}$, $St^+_{1/C}$ and St^+_F are respectively plotted as a function of hydraulic properties.

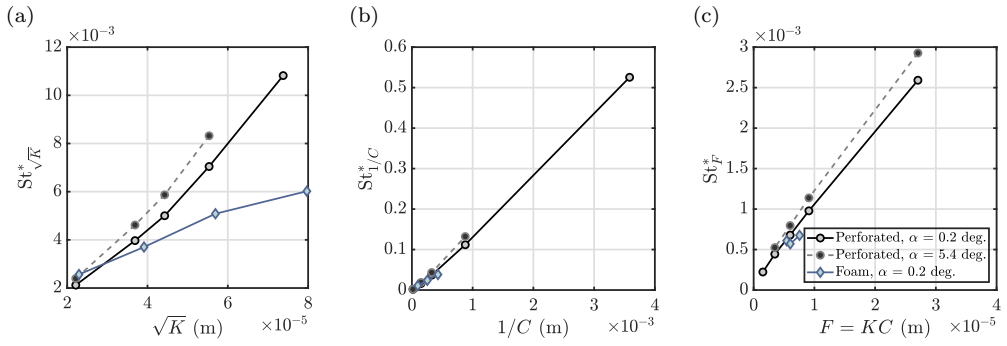

Fig. A.1. Scaling of St^*_c with length scales derived from the permeability characterization. (a) $\sqrt{K}$. (b) $1/C$. (c) $F = KC$.

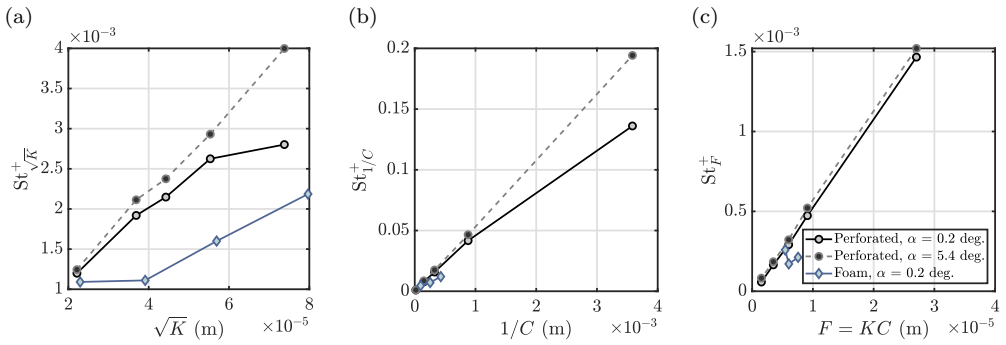

Fig. A.2. Scaling of St^+ with length scales derived from the permeability characterization. (a) $\sqrt{K}$. (b) $1/C$. (c) $F = KC$.

Appendix B. Fitting Coefficients

For completeness, the coefficients employed for the fit of experimental data to Eqs. (5), (8) and (9) are respectively presented in Tables B.1, B.2 and B.3, together with the coefficient of determination R^2, that gives a measure of the goodness of the fit.

Table B.1
Coefficients (γ_1, γ_2) (with 95% confidence bounds) and correlation coefficient R^2 for the fit of experimental $\Delta L_{p,\max}$ and K data to Eq. (5).

Case	γ_1 (dB)	$\gamma_2 \times 10^{-9}$ (m^{-2})	R^2
Perforated, $\alpha = 0.2$ deg.	9.311 ± 0.984	0.388 ± 0.084	0.995
Perforated, $\alpha = 5.4$ deg.	7.310 ± 0.699	0.456 ± 0.098	0.988
Metal Foam, $\alpha = 0.2$ deg	9.358 ± 1.221	1.484 ± 0.779	0.943

Table B.2
Coefficients (χ_1, χ_2) (with 95% confidence bounds) and correlation coefficient R^2 for the fit of experimental m and K data to Eq. (8).

$\chi_1 \times 10^{-9}$ (m^{-2})	χ_2 (-)	R^2
23.306 ± 7.535	5.215 ± 0.142	0.8575

Table B.3
Coefficients (ξ_1, ξ_2) (with 95% confidence bounds) and correlation coefficient R^2 for the fit of experimental $\Delta L_{p,\max}$ and s/c data to Eq. (9).

Case	ξ_1 (dB)	ξ_2 (-)	R^2
$l_h = 5$ mm ($K = 5 \times 10^{-10}$ m^2)	2.117 ± 0.964	19.834 ± 32.040	0.945
$l_h = 2$ mm ($K = 31 \times 10^{-10}$ m^2)	7.553 ± 2.513	27.923 ± 50.391	0.869

References

[1] S. Oerlemans, P. Sijtsma, B.M. López, Location and quantification of noise sources on a wind turbine, J. Sound Vib. (2007), doi:10.1016/j.jsv.2006.07.032.
[2] S. Moreau, B. Dignou, P. Jaiswal, G.R. Yakhina, Y. Pasco, M. Sanjose, B. Alstrom, N. Atalla, Trailing-edge noise of a flat plate with several liner-type porous appendices, in: 2018 AIAA/CEAS Aeroacoustics Conference, 2018, pp. 1–14, doi:10.2514/6.2018-3119.
[3] J.F. Piet, R. Davy, G. Elias, H. Siller, L. Chow, C. Seror, F. Laporte, Flight test investigation of add-on treatments to reduce aircraft airframe noise, in: 11th AIAA/CEAS Aeroacoustics Conference, 2005, pp. 1–20, doi:10.2514/6.2005-3007.
[4] M.S. Howe, Trailing edge noise at low mach numbers, J. Sound Vib. 225 (2) (1999) 211–238, doi:10.1006/jsvi.1999.2236.
[5] T. Geyer, E. Sarradj, C. Fritzsche, Measurement of the noise generation at the trailing edge of porous airfoils, Exp. Fluids 48 (2) (2010) 291–308, doi:10.1007/s00348-009-0739-x.
[6] T. Geyer, E. Sarradj, Noise generation by porous airfoils, in: 13th AIAA/CEAS Aeroacoustics Conference, 2007, doi:10.2514/6.2007-3719.
[7] J. Delfs, B. Faßmann, N. Lippitz, M. Lummer, M. Mößner, L. Müller, K. Rurkowska, S. Uphoff, SFB 880: aeroacoustic research for low noise take-off and landing, CEAS Aeronaut. J. 5 (4) (2014) 403–417, doi:10.1007/s13272-014-0115-2.
[8] A. Kisil, L.J. Ayton, Aerodynamic noise from rigid trailing edges with finite porous extensions, J. Fluid Mech. 836 (11) (2018) 117–144, doi:10.1017/jfm.2017.782.
[9] A.R. Carpio, F. Avallone, D. Ragni, M. Snellen, S.V.D. Zwaag, Mechanisms of broadband noise generation on metal foam edges, Phys. Fluids 31 (10) (2019), doi:10.1063/1.5121248.

[10] T. Geyer, E. Sarradj, C. Fritzsche, Porous airfoils: noise reduction and boundary layer effects, Int. J. Aeroacoust. 9 (6) (2010) 787–820, doi:10.1260/1475-472x.9.6.787.
[11] M. Herr, K.S. Rossignol, J. Delfs, N. Lippitz, M. Moßner, Specification of porous materials for low-noise trailing-edge applications, in: 20th AIAA/CEAS Aeroacoustics Conference, 2014, pp. 1–19, doi:10.2514/6.2014-3041.
[12] A.R. Carpio, R.M. Martínez, F. Avallone, D. Ragni, M. Snellen, S. van der Zwaag, Experimental characterization of the turbulent boundary layer over a porous trailing edge for noise abatement, Journal of Sound and Vibration 443 (2019) 537–558, doi:10.1016/j.jsv.2018.12.010. 3
[13] T.F. Geyer, E. Sarradj, Self noise reduction and aerodynamics of airfoils with porous trailing edges, Acoustics 1 (2) (2019) 393–409, doi:10.3390/acoustics1020022. ISSN 2624-599X
[14] M. Herr, J. Reichenberger, In search of airworthy trailing-edge noise reduction means, in: 17th AIAA/CEAS Aeroacoustics Conference, 2011, pp. 1–25, doi:10.2514/6.2011-2780. Number June
[15] S.A.S. Ali, M. Azarpeyvand, C.R.I.D. Silva, Trailing-edge flow and noise control using porous treatments, Journal of Fluid Mechanics 850 (2018) 83–119, doi:10.1017/jfm.2018.430. June 2017
[16] I. Gibson, D. Rosen, B. Stucker, Additive Manufacturing Technologies, Springer, New York, New York, NY, 2015, doi:10.1007/978-1-4939-2113-3. ISBN 978-1-4939-2112-6
[17] C. Jiang, D. Moreau, Y. Yauwenas, J.R. Fischer, C.J. Doolan, J. Gao, W. Jiang, R. McKay, M. Kingan, Control of rotor trailing edge noise using porous additively manufactured blades, in: 2018 AIAA/CEAS Aeroacoustics Conference, 2018, pp. 1–24, doi:10.2514/6.2018-3792.
[18] M. Drela, XFOIL: an analysis and design system for low Reynolds number airfoils, in: Low Reynolds Number Aerodynamics, 1989, pp. 1–12, doi:10.1007/978-3-642-84010-4.
[19] C. Teruna, F. Manegar, F. Avallone, D. Casalino, D. Ragni, A.R. Carpio, T. Carolus, Numerical analysis of metal-foam application for trailing edge noise reduction, in: 25th AIAA/CEAS Aeroacoustics Conference, 2019, 2019, doi:10.2514/6.2019-2650.
[20] EnvisionTEC GmbH, Htm 140 v2 technical datasheet, 2018.
[21] J. Kennedy, L. Flanagan, L. Dowling, G.J. Bennett, H. Rice, D. Trimble, The influence of additive manufacturing processes on the performance of a periodic acoustic metamaterial, Int. J. Polym. Sci. 2019 (i) (2019) 1–11, doi:10.1155/2019/7029143.
[22] D. Ingham, I. Pop, Transport Phenomena in Porous Media, Pergamon, 1998, doi:10.1016/B978-0-08-042843-7.X5000-4. ISBN 978-0-08-042843-7
[23] A.R. Carpio, R. Merino-Martínez, F. Avallone, D. Ragni, M. Snellen, S. van der Zwaag, Broadband trailing edge noise reduction using permeable metal foams, in: 46th International Congress and Exposition of Noise Control Engineering, 27–30 August, 2017, Hong Kong, 2017, pp. 4373–4383.
[24] Y. Bae, Y.I. Kim, Numerical modeling of anisotropic drag for a perforated plate with cylindrical holes, Chem. Eng. Sci. 149 (2016) 78–87, doi:10.1016/j.ces.2016.04.036.
[25] A.R. Carpio, F. Avallone, D. Ragni, M. Snellen, S. van der Zwaag, 3D-printed Perforated Trailing Edges for Broadband Noise Abatement, in: 25th AIAA/CEAS Aeroacoustics Conference, 2019, pp. 1–13, doi:10.2514/6.2019-2458.
[26] P. Grathwohl, Diffusion in natural porous media: Contaminant transport, sorption/desorption and dissolution kinetics, volume 1 of Topics in Environmental Fluid Mechanics, first ed., Springer US, Boston, MA, 1998, doi:10.1007/978-1-4615-5683-1. ISBN 978-0-7923-8102-0
[27] B. Tjaden, D.J.L. Brett, P.R. Shearing, Tortuosity in electrochemical devices: a review of calculation approaches, Int. Mater. Rev. 63 (2) (2018) 47–67, doi:10.1080/09506608.2016.1249995.
[28] N. Epstein, On tortuosity and the tortuosity factor in flow and diffusion through porous media, Chem. Eng. Sci. 44 (3) (1989) 777–779, doi:10.1016/0009-2509(89)85053-5.
[29] E.A. Codling, M.J. Plank, S. Benhamou, Random walk models in biology, J. R. Soc. Interface 5 (25) (2008) 813–834, doi:10.1098/rsif.2008.0014.
[30] T.G. Tranter, M.D.R. Kok, M. Lam, J.T. Gostick, pytrax: a simple and efficient random walk implementation for calculating the directional tortuosity of images, SoftwareX 10 (2019) 100277, doi:10.1016/j.softx.2019.100277.
[31] H. Iwai, N. Shikazono, T. Matsui, H. Teshima, M. Kishimoto, R. Kishida, D. Hayashi, K. Matsuzaki, D. Kanno, M. Saito, H. Muroyama, K. Eguchi, N. Kasagi, H. Yoshida, Quantification of ni-YSZ anode microstructure based on dual beam FIB-SEM technique, ECS Trans. 25 (2) (2009) 1819–1828, doi:10.1149/1.3205723.
[32] J.M. Zalc, S.C. Reyes, E. Iglesia, The effects of diffusion mechanism and void structure on transport rates and tortuosity factors in complex porous structures, Chem. Eng. Sci. 59 (14) (2004) 2947–2960, doi:10.1016/j.ces.2004.04.028.
[33] P.D. Plessis, A. Montillet, J. Comiti, J. Legrand, Pressure drop prediction for flow through high porosity metallic foams, Chem. Eng. Sci. 49 (21) (1994) 3545–3553, doi:10.1016/0009-2509(94)00170-7.
[34] B.P. Boudreau, The diffusive tortuosity of fine-grained unlithified sediments, Geochim. Cosmochim. Acta 60 (16) (1996) 3139–3142, doi:10.1016/0016-7037(96)00158-5.
[35] K.K. Bodla, J.Y. Murthy, S.V. Garimella, Microtomography-based simulation of transport through open-cell metal foams, Numer. Heat Transf. Part A 58 (7) (2010) 527–544, doi:10.1080/10407782.2010.511987.
[36] S. Moreau, M. Henner, G. Iaccarino, M. Wang, M. Roger, Analysis of flow conditions in freejet experiments for studying airfoil self-noise, AIAA Journal 41 (10) (2003) 1895–1905, doi:10.2514/2.1905. 10
[37] G. Iosilevskii, Aerodynamics of permeable membrane wings, European Journal of Mechanics - B/Fluids 30 (5) (2011) 534–542, doi:10.1016/j.euromechflu.2011.05.003. 9
[38] M. Aldheeb, W. Asrar, E. Sulaeman, A.A. Omar, Aerodynamics of porous airfoils and wings, Acta Mech. 229 (9) (2018) 3915–3933, doi:10.1007/s00707-018-2203-6.
[39] F. Wienke, A. Dillmann, M. Raffel, Experimental investigation of the influence of permeability on finite wing lift and drag, in: New Results in Numerical and Experimental Fluid Mechanics XII, first ed., Springer International Publishing, 2020, pp. 716–725, doi:10.1007/978-3-030-25253-3_68.
[40] S. Luesutthiviboon, A. Malgoezar, M. Snellen, P. Sijtsma, D. Simons, Improving source discrimination performance by using an optimized acoustic array and adaptive high-resolution CLEAN-SC Beamforming, in: 7th Berlin Beamforming Conference, 2018.
[41] P. Welch, The use of fast fourier transform for the estimation of power spectra: A method based on time averaging over short, modified periodograms, IEEE Transactions on Audio and Electroacoustics 15 (2) (1967) 70–73. 6 doi: 10.1109/TAU.1967.1161901.
[42] P. Sijtsma, Phased Array Beamforming Applied to Wind Tunnel and Fly-Over Tests, Technical Report October, NLR, 2010.
[43] R. Merino-Martínez, P. Sijtsma, M. Snellen, T. Ahlefeldt, J. Antoni, C.J. Bahr, D. Blacodon, D. Ernst, A. Finez, S. Funke, T.F. Geyer, S. Haxter, G. Herold, X. Huang, W.M. Humphreys, Q. Leclère, A. Malgoezar, U. Michel, T. Padois, A. Pereira, C. Picard, E. Sarradj, H. Siller, D.G. Simons, C. Spehr, A Review of Acoustic Imaging Methods using Phased Microphone Arrays: Part of the “Aircraft Noise Generation and Assessment” Special Issue, 10, Springer, Vienna, 2019, doi:10.1007/s13272-019-00383-4.
[44] P. Chiariotti, M. Martarelli, P. Castellini, Acoustic beamforming for noise source localization - reviews, methodology and applications, Mech. Syst. Signal Process. 120 (2019) 422–448, doi:10.1016/j.ymssp.2018.09.019.
[45] R. Merino-Martínez, P. Sijtsma, A.R. Carpio, R. Zamponi, S. Luesutthiviboon, A.M.N. Malgoezar, M. Snellen, C. Schram, D.G. Simons, Integration methods for distributed sound sources, Int. J. Aeroacoust. (2019), doi:10.1177/1475472X19852945.
[46] S. Oerlemans, P. Migliore, Aeroacoustic wind tunnel tests of wind turbine airfoils, in: 10th AIAA/CEAS Aeroacoustics Conference, 2004, pp. 1–18, doi:10.2514/6.2004-3042.
[47] E. Sarradj, G. Herold, P. Sijtsma, R.M. Martinez, T.F. Geyer, C.J. Bahr, R. Porteous, D. Moreau, C.J. Doolan, A microphone array method benchmarking exercise using synthesized input data, in: 23rd AIAA/CEAS Aeroacoustics Conference, 2017, pp. 1–16, doi:10.2514/6.2017-3719.
[48] S. Oerlemans, P. Sijtsma, Determination of absolute levels from phased array measurements using spatial source coherence, in: 8th AIAA/CEAS Aeroacoustics Conference & Exhibit, 2002, pp. 1–12, doi:10.2514/6.2002-2464.
[49] E. Sarradj, T. Geyer, Symbolic regression modeling of noise generation at porous airfoils, J. Sound Vib. 333 (14) (2014) 3189–3202, doi:10.1016/j.jsv.2014.02.037.

[50] C. de Boor, A Practical Guide to Splines, 27, Springer-Verlag, New York, 1978. ISBN 978-0-387-95366-3
[51] B.A. Barsky, T.D. DeRose, Geometric continuity of parametric curves: three equivalent characterizations, IEEE Computer Graphics and Applications 9 (6) (1989) 60–69, doi:10.1109/38.41470. 11
[52] W.J. Devenport, D.L. Grissom, W. Nathan, A. B. S. Smith, S.A.L. Glegg, Measurements of roughness noise, J. Sound Vib. 330 (17) (2011) 4250–4273, doi:10.1016/j.jsv.2011.03.017.
[53] H.Y. Gao, Y.H. He, J. Zou, N.P. Xu, C.T. Liu, Tortuosity factor for porous feal intermetallics fabricated by reactive synthesis, Trans. Nonferrous Metals Soc. China 22 (9) (2012) 2179–2183, doi:10.1016/S1003-6326(11)61446-5.
[54] S. Pardo-Alonso, J. Vicente, E. Solórzano, M.A. Rodriguez-Perez, D. Lehmhus, Geometrical tortuosity 3d calculations in infiltrated aluminium cellular materials, Procedia Mater. Sci. 4 (2014) 145–150, doi:10.1016/j.mspro.2014.07.553.
[55] B. Moore, Hearing, Elsevier Science, 1995. ISBN 9780125056267
[56] J.E. Ffowcs-Williams, L.H. Hall, Aerodynamic sound generation by turbulent flow in the vicinity of a scattering half plane, Journal of Fluid Mechanics 40 (04) (1970) 57, doi:10.1017/s0022112070000368. 6
[57] M.S. Howe, Aerodynamic noise of a serrated trailing edge, J Fluids Struct. 5 (1) (1991) 33–45, doi:10.1016/0889-9746(91)80010-B.
[58] T.F. Brooks, D.S. Pope, M.A. Marcolini, Airfoil Self-Noise and Prediction, Technical report, NASA Langley Research Center, 1989.
[59] M. Mößner, R. Radespiel, Flow simulations over porous media - comparisons with experiments, Comput. Fluids 154 (2017) 358–370, doi:10.1016/j.compfluid.2017.03.002.